Molecular Cell

Article

Retron-Eco1 assembles NAD$^+$-hydrolyzing filaments that provide immunity against bacteriophages

Graphical abstract

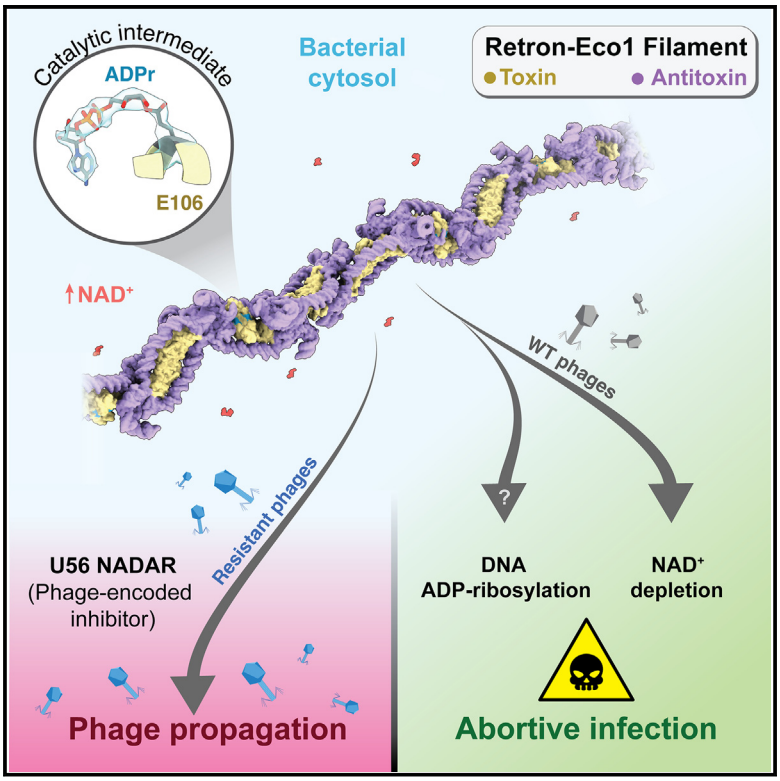

Highlights

- Retron-Eco1 assembles NAD$^+$-hydrolyzing filaments at cellular NAD$^+$ concentrations
- The filaments trap the effector in a non-toxic catalytic intermediate state
- Retron-Eco1 leads to NAD$^+$ depletion upon phage infection
- U56 is a phage-encoded inhibitor that binds the NAD$^+$ hydrolysis product ADPr

Authors

Arturo Carabias,
Sarah Camara-Wilpert,
Mario Rodríguez Mestre, ...,
Michael L. Nielsen,
Rafael Pinilla-Redondo,
Guillermo Montoya

Correspondence

arturo.cdr@cpr.ku.dk (A.C.),
rafael.pinilla@bio.ku.dk (R.P.-R.),
guillermo.montoya@cpr.ku.dk (G.M.)

In brief

Retrons are bacterial immune systems against their parasites (bacteriophages). Carabias et al. explore the immune mechanism of Retron-Eco1, showing that it forms filaments that consume NAD$^+$ during infection. The authors also shed light on the mechanisms of bacteriophage immune evasion by finding a bacteriophage-encoded inhibitor that binds an NAD$^+$-related molecule.

Carabias et al., 2024, Molecular Cell *84*, 2185–2202
June 6, 2024
https://doi.org/10.1016/j.molcel.2024.05.001

CellPress

Molecular Cell

CellPress

Article

Retron-Eco1 assembles NAD$^+$-hydrolyzing filaments that provide immunity against bacteriophages

Arturo Carabias,[1,*] Sarah Camara-Wilpert,[2] Mario Rodríguez Mestre,[2,6] Blanca Lopéz-Méndez,[3,6] Ivo A. Hendriks,[4,6] Ruiliang Zhao,[2] Tillmann Pape,[1,5] Anders Fuglsang,[1] Sean Hoi-Ching Luk,[1] Michael L. Nielsen,[4] Rafael Pinilla-Redondo,[2,*] and Guillermo Montoya[1,7,*]

[1]Structural Molecular Biology Group, Novo Nordisk Foundation Centre for Protein Research, Faculty of Health and Medical Sciences, University of Copenhagen, Blegdamsvej 3B, 2200 Copenhagen, Denmark

[2]Section of Microbiology, Department of Biology, University of Copenhagen, 2100 Copenhagen, Denmark

[3]Protein Purification and Characterization Facility, Novo Nordisk Foundation Center for Protein Research, Faculty of Health and Medical Sciences, University of Copenhagen, 2200 Copenhagen, Denmark

[4]Proteomics Department, Novo Nordisk Foundation Center for Protein Research, Faculty of Health and Medical Sciences, University of Copenhagen, 2200 Copenhagen, Denmark

[5]Core Facility for Integrated Microscopy (CFIM), Faculty of Health and Medical Sciences, University of Copenhagen, 2200 Copenhagen, Denmark

[6]These authors contributed equally

[7]Lead contact

*Correspondence: arturo.cdr@cpr.ku.dk (A.C.), rafael.pinilla@bio.ku.dk (R.P.-R.), guillermo.montoya@cpr.ku.dk (G.M.)

https://doi.org/10.1016/j.molcel.2024.05.001

SUMMARY

Retrons are toxin-antitoxin systems protecting bacteria against bacteriophages via abortive infection. The Retron-Eco1 antitoxin is formed by a reverse transcriptase (RT) and a non-coding RNA (ncRNA)/multi-copy single-stranded DNA (msDNA) hybrid that neutralizes an uncharacterized toxic effector. Yet, the molecular mechanisms underlying phage defense remain unknown. Here, we show that the *N*-glycosidase effector, which belongs to the STIR superfamily, hydrolyzes NAD$^+$ during infection. Cryoelectron microscopy (cryo-EM) analysis shows that the msDNA stabilizes a filament that cages the effector in a low-activity state in which ADPr, a NAD$^+$ hydrolysis product, is covalently linked to the catalytic E106 residue. Mutations shortening the msDNA induce filament disassembly and the effector's toxicity, underscoring the msDNA role in immunity. Furthermore, we discovered a phage-encoded Retron-Eco1 inhibitor (U56) that binds ADPr, highlighting the intricate interplay between retron systems and phage evolution. Our work outlines the structural basis of Retron-Eco1 defense, uncovering ADPr's pivotal role in immunity.

INTRODUCTION

Prokaryotes have evolved diverse defense systems against invading genetic parasites, such as bacteriophages (phages) and plasmids. Some systems target the invader directly,[1–6] while others activate abortive infection (Abi) mechanisms, in which the infected cells become dormant or die to prevent the spread of the infection throughout the population.[7] During Abi, sensing of infection induces the activation of an effector module that causes cell toxicity through diverse mechanisms,[4,7] and depletion of NAD$^+$ is emerging as a common strategy.[8–13] A well-reported example is the Thoeris system, in which ThsA protein depletes NAD$^+$ after being activated by a 1″-3′ glycocyclic adenosine 5′-diphosphate ribose (1′-3′ gcADPR) signal produced by ThsB.[8,9] Interestingly, NAD$^+$-degrading modules are similarly prevalent in eukaryotic immunity, highlighting parallelisms across the tree of life.[14] Other prokaryotic NAD$^+$-hydrolyzing enzymes induce toxicity by linking adenosine 5′-diphosphate ribose (ADPr), the product of NAD$^+$ hydrolysis, to different targets (reviewed in Mikolčević et al.[15]). A well-characterized case is the DarT/G anti-phage defense system,[16] in which Dart1 and Dart2 ADP-ribosyl transferases (ARTs) transfer ADPr to G and T bases, respectively.[17,18] This modification induces DNA damage response and impacts replication and likely transcription processes.[19] The toxic effect of the ADPr transfer is neutralized by the antitoxins DarG1 and DarG2, which are NADAR (NAD and ADP-ribose) domain- and macrodomain-containing proteins that hydrolyze the ADPr-base *N*-glycosidic bond generated by DarT1 and DarT2 ARTs, respectively.[17,18]

Retrons are prokaryotic genetic retroelements that mediate Abi upon phage infection.[20–22] They encode a reverse transcriptase (RT), a non-coding RNA (ncRNA), and one or several effector enzymes.[23] The RT produces a multi-copy single-stranded DNA (msDNA) from the ncRNA template.[24] This property has been applied in gene editing and synthetic biology.[25–28] The ncRNA gene comprises the *a1 and a2*

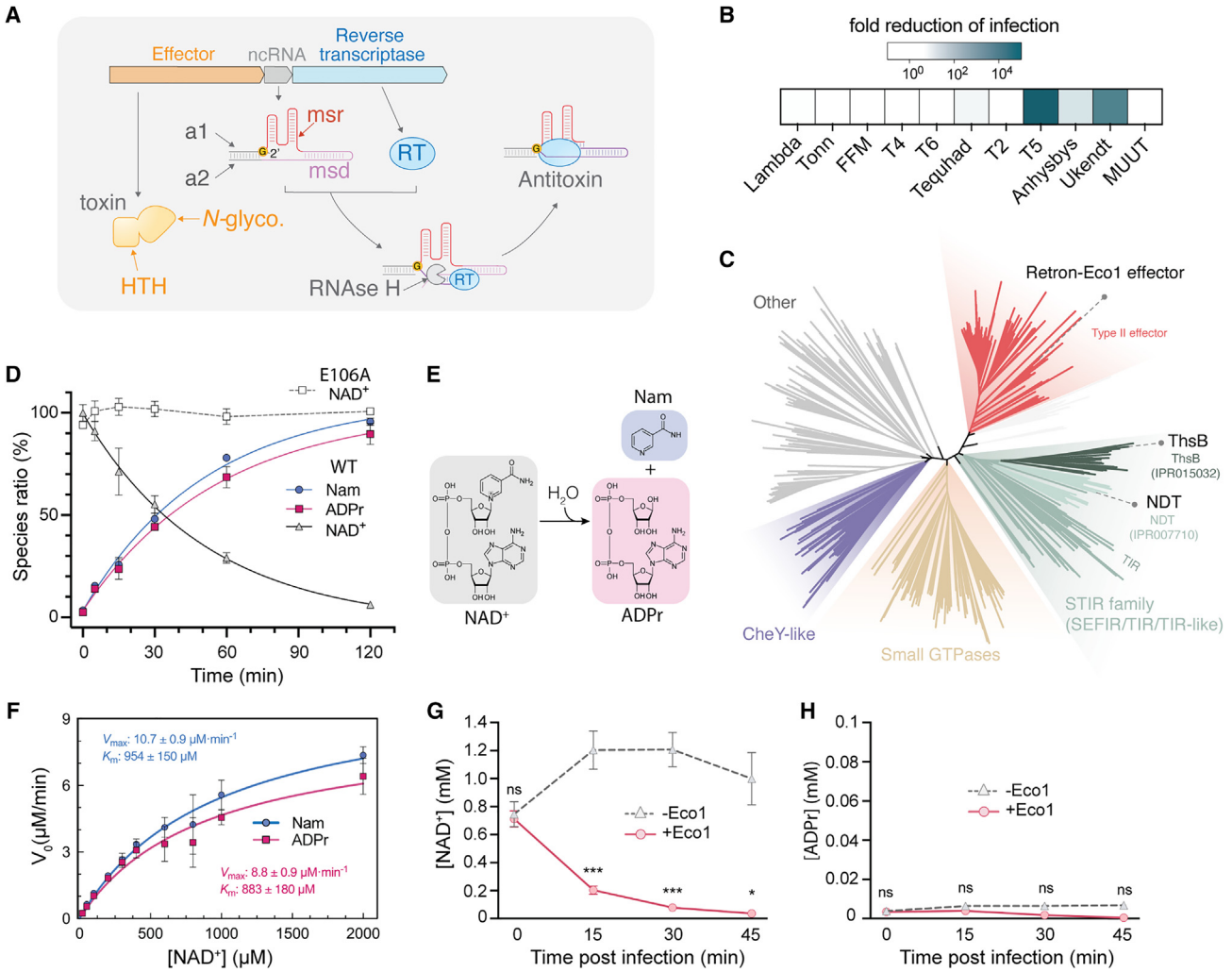

Figure 1. Retron-Eco1 depletes NAD$^+$ upon phage infection

(A) Overview of Retron-Eco1 (Ec86) toxin-antitoxin system, depicting the reverse transcriptase (RT), ncRNA, and effector with predicted *N*-glycosidase activity.

(B) Heatmap illustrating the level of defense provided by Retron-Eco1 against specific phages. The 10-fold reductions of infection relative to the empty vector control are plotted (see also Figure S1).

(C) Structure-based tree of the Retron-Eco1 effector and structural homologs. The positions of the Retron-Eco1 *N*-glycosidase domain, NDT (PDB: 1F8Y), and ThsB (PDB: 6LHY) are highlighted.

(D) In vitro NAD$^+$ degradation assay using recombinant Retron-Eco1-WT and E106A effector inactive mutant. Data represent independent experiments (n = 3) plotted as the mean ± standard deviation (SD) (see also Table S1).

(E) Schematic of NAD$^+$ hydrolysis, as measured in (D).

(F) Kinetic analysis of Retron-Eco1. V_{max} and K_m values were determined by fitting a Michaelis-Menten equation to the experimental data for ADPr and Nam. Data represent independent experiments (n = 3) plotted as the mean ± standard deviation (SD).

(G and H) Quantification of the cellular NAD$^+$ and ADPr concentration after phage infection. *E. coli* MG1655 lacking or carrying Retron-Eco1 was infected with T5 phage, and the levels of NAD$^+$(G) and ADPr (H) were measured by liquid chromatography-tandem mass spectrometry (LC-MS/MS). Data are shown as the mean ± standard deviation (SD) of three biological replicates (n = 3). Statistical analysis was performed by an unpaired t test with Welch's correction for each time in (G) and (H). ns, non-significant, *p < 0.05, ***p < 0.005.

segments, as well as the coding regions for msdRNA (*msr*) and msDNA (*msd*) (Figure 1A). The a1 segment primes the RT, which creates an initial 2′-5′ phosphodiester bond between the first nucleotide and the conserved branching guanosine (bG) (Figure 1A). Then, the RT generates the msDNA using the msd RNA template while the host RNase H1 degrades the msd RNA,[29] a process that influences reverse transcription termination.[30] Retron-Eco1 msr-msDNA hybrid product remains intact and forms a complex with the RT.[30,31] Recent research on Retron-Sen2 supports that the type II family retrons are DNA-containing toxin-antitoxin systems in which the effector's *N*-glycosidase (*N*-glyco) domain is the toxin, and the RT-msr-msDNA is the antitoxin[20] (Figure 1A). Structural and functional evidence of the related Retron-Eco1 confirms the

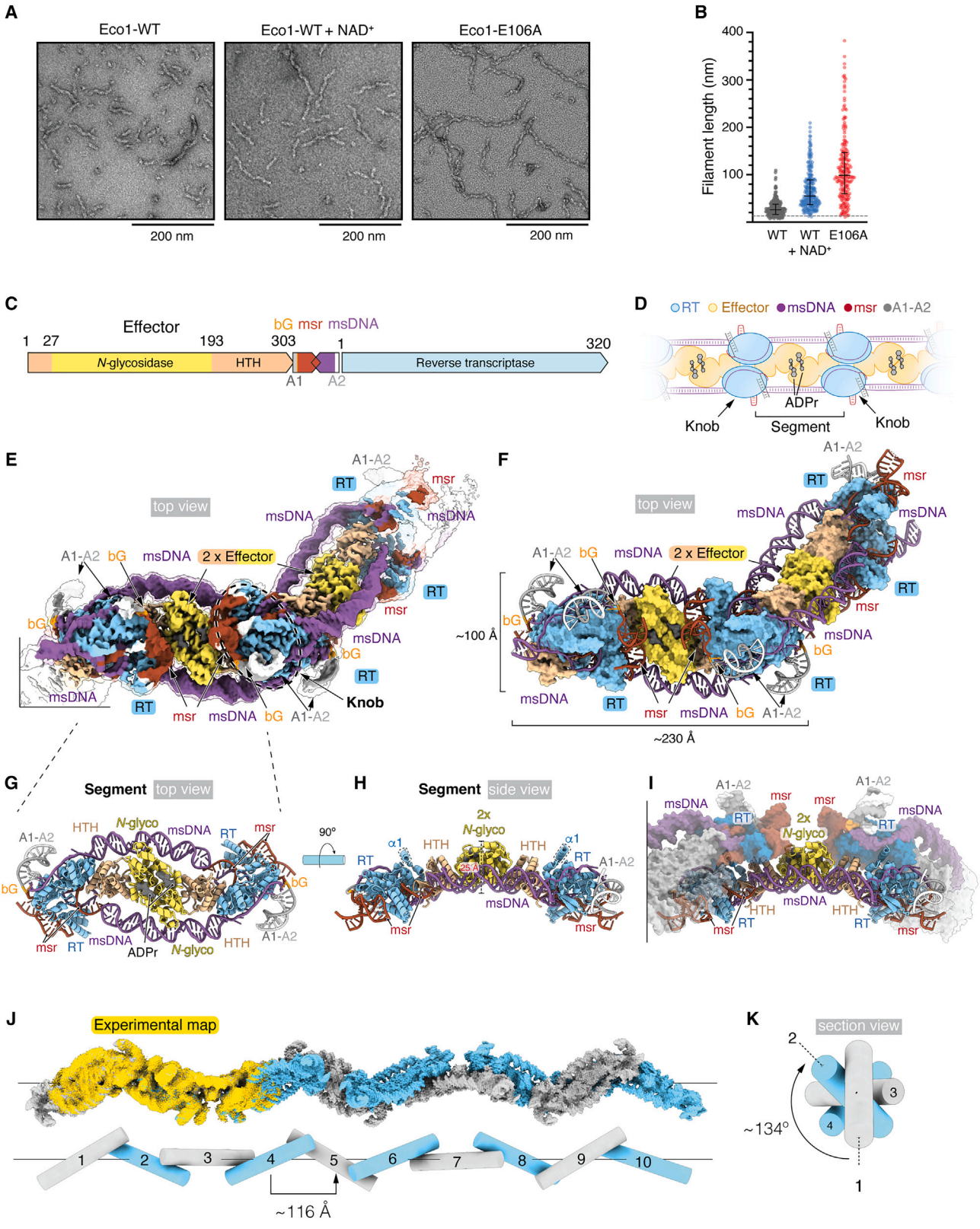

(legend on next page)

complex formation and reveals the interactions between the toxin and antitoxin.[31] However, the type II retron family Abi mechanism remains enigmatic.

Here, we reveal that NAD^+ is the substrate of the *N*-glyco domain and show that Retron-Eco1 induces NAD^+ depletion during phage infection. Incubation with NAD^+ stimulates the assembly of long filaments encapsulating the effector in a catalytically suboptimal state. Intriguingly, we found two ADPr molecules covalently linked to the effector's E106 catalytic residue, which represents an intermediate step of the enzymatic reaction. Thus, Retron-Eco1 filaments are primed. We also present the structure of a toxic variant, unveiling how shorter msDNAs lead to filament instability and effector toxicity. Notably, the expression of the toxic mutants results in the transfer of ADPr to the DNA, implying that Retron-Eco1-mediated DNA ADP-ribosylation could also contribute to Abi. Furthermore, we identified a phage-encoded Retron-Eco1 inhibitor (U56). U56 is a NADAR protein that binds ADPr, and we show that the previously described NADAR hydrolytic activity is dispensable for U56-mediated inhibition. This suggests that U56's mechanism likely involves the binding to ADPr or ADPr-linked molecules.

RESULTS

Retron-Eco1 provides immunity against T5 and phi-92-like phages

First, we sought to identify phages that trigger Retron-Eco1 immune activity. We challenged *E. coli* cells expressing Retron-Eco1 with a diverse panel of coliphages and found robust protection against T5 and phi-92-like phages (Ukendt and Anhysbys[32]) (Figures 1B, S1A, and S1B; STAR Methods). Growth curves of *E. coli* cultures containing Retron-Eco1 further revealed that the bacterial population collapsed when cells were infected at high multiplicity of infection (MOI), akin to cells lacking Retron-Eco1. On the other hand, the cultures kept growing normally when subjected to low MOI, whereas Retron-Eco1-lacking cells collapsed under the same conditions. These results confirm that the presence of Retron-Eco1 effectively protects *E. coli* cells through an Abi mechanism[21] (Figure S1C).

The Retron-Eco1 effector protein hydrolyzes NAD^+

The type II retron effectors contain nucleoside 2-deoxyribosyltransferase-like (NDT) domains with predicted *N*-glyco activity, which are essential for phage defense.[20–22] However, the substrate specificity of the *N*-glyco domain remained elusive. To address this question, we performed a structure-based phylogenetic study, which revealed that the type II retron *N*-glyco domains constitute a separate group within the SEFIR/TIR/SEFIR-TIR-like (STIR) superfamily of NAD^+-processing enzymes (STAR Methods; Figure 1C).

The structural similarities with other STIR members led us to speculate that the *N*-glyco domain could hydrolyze NAD^+. We tested this hypothesis biochemically by producing a recombinant wild-type (WT) Retron-Eco1 and incubating it in the presence of NAD^+ (Figure S1D; STAR Methods). Retron-Eco1 hydrolyzed the nicotinamide (Nam)–ribosyl bond of NAD^+, generating Nam and ADPr, and no other products of the NAD^+-ADPr network observed in other virus-host interactions[33] were detected in the reaction mixture (Figures 1D, 1E, and S1E; STAR Methods; Table S1). The *N*-glyco-inactivating mutation E106A abrogated NAD^+ cleavage, confirming the *N*-glyco hydrolytic activity (Figures 1D, 1E, and S1E). We further characterized the activity kinetically by determining the K_m and V_{max} values based on the ADPr and Nam production rates. The K_m was consistent with NAD^+ concentrations previously estimated in *E. coli* (~200–640 μM), supporting the enzyme's ability to hydrolyze NAD^+ under cellular conditions.[34,35] However, Retron-Eco1's V_{max} was notably slower than that of other NAD^+-degrading enzymes involved in phage defense (Figure 1F), e.g., 6–8 times slower than the Thoeris ThsA NAD^+ hydrolase (V_{max} of 67.69 μmol/min).[36]

To further investigate the effector's activity during immunity, we quantified the cellular NAD^+ content at different times after infection with T5 phage (Figure 1G; STAR Methods). The NAD^+ levels remained high during infection in Retron-Eco1-lacking cells. However, Retron-Eco1-containing cells experienced a decrease in the cellular NAD^+ concentration that reached minimum levels (<80 μM) after 30 min of infection. This profile is comparable to NAD^+ depletion trends observed in other Abi bacterial defense mechanisms,[13] supporting its contribution to Abi. Intriguingly, we did not detect the accumulation of two possible products of the reaction, ADPr or cyclic ADP-ribose (cADPr), suggesting that these metabolites are either further processed or transferred to other moieties (Figures 1H and S1F).

Retron-Eco1 assembles filaments

To gain molecular insights into the NAD^+ hydrolysis, we studied the structure of Retron-Eco1 complexes in the absence and presence of NAD^+ (Figures 2A, 2B, and S2A). Retron-Eco1 eluted as a wide peak by size exclusion chromatography (SEC) revealing the heterogeneity of the complex (Figure S2A), and

Figure 2. Retron-Eco1 form filamentous structures

(A) Negative staining analysis of Retron-Eco1 in the absence or presence of NAD^+ and E106A mutant. The scalebars represent 200 nm.

(B) Quantification of the filament length from the negative staining data shown in (A). The horizontal dashed line represents the dimension of the "dimeric" complex[31] (13 nm). Data represent ~n = 200 particles plotted as median ± interquartile range.

(C) Schematic of the primary sequence of the Retron-Eco1 cassette.

(D) Cartoon model of the filament assembly.

(E) Cryo-EM map of Retron-Eco1 (E106A) displaying two segments of the filament (see also Figures S2–S6). The semi-transparent envelope corresponds to the map at a low contour level (sigma 0.15).

(F) Atomic model of Retron-Eco1 (E106A) filament.

(G and H) Architecture of a segment of the WT filament, containing 2× RT, 2× ncRNA-msDNA, and 2× effector protein. Two ADPr molecules are labeled in the two *N*-glycosidase catalytic sites.

(I) Side view of a three-segment model of the filament.

(J and K) 10-Segment filament model generated by applying the helical parameters determined from the Retron-Eco1 cryo-EM maps.

negative staining analysis revealed that a significant fraction of the Retron-Eco1 particles (>50%) exhibited filament-like assemblies of ~14-nm width and some of them extending up to ~100 nm in length. By contrast, a few particles matched the reported Retron-Eco1 complex structure comprising a dimer (90 × 130 Å)[31] (Figures 2A and 2B). Incubation of Retron-Eco1 with 1 mM NAD^+ resulted in a shift of the peak toward the SEC column void volume (Figure S2A), and negative staining confirmed the formation of open-ended higher-order filamentous structures (Figures 2A and 2B). Interestingly, the E106A mutant formed longer filaments in the absence of NAD^+ (up to ~400 nm in length), while the diameter was comparable to the WT particles (Figures 2A and 2B). Hence, the incubation of Retron-Eco1 with NAD^+ promotes filamentous assembly of the WT complexes, whereas the catalytically inactive mutant E106A appears to exist solely in the filamentous form.

Architecture of Retron-Eco1 filament assembly

To dissect the catalytic mechanism of Retron-Eco1, we determined three cryoelectron microscopy (cryo-EM) structures (Figures 1A, 2A, 2C, S1D, S2B–S2F, S3, and S4A–S4D). Two structures correspond to Retron-Eco1-WT in the absence and presence of NAD^+ (at 4.4 and 3.1 Å overall resolution) and the third to the catalytically inactive E106A mutant (at 2.7 Å overall resolution) (Figures 2D–2F and S2–S4; Table S2; STAR Methods). The structures revealed that the filament consists of an assembly of the previously reported Retron-Eco1 dimers[31] that build the "knobs" (Figures 2D–2F). The retron dimer is stabilized by interactions of the helix α1 of one RT protomer with a surface formed by the other and the nucleotides dA4, dG5, and dA6 of the msr-msDNA hybrid[31] (Figures S5A and S5B). Attempts to truncate the helix α1 (Δ14) strongly compromised the msDNA production, supporting its essential role for reverse transcription and suggesting possible alterations in protein stability or its dimeric assembly (Figure S5C). This mutant also affected the phage defense phenotype, in agreement with the essential msDNA's role for immunity[20–22,31] (Figure S5D).

The assembly of the retron dimers in the filament positions the msDNA stem-loops in a staggered arrangement that builds a scaffold encapsulating effector dimers along the axial axis of the filament (Figures 2D–2H). Therefore, the filament is formed by a repeating segment that extends from knob to knob (Figures 2D and 2G–2I). Moreover, our structures provide the basis to generate a model of the helical filaments, displaying a helical pitch of ~116 Å along the longitudinal axis and a rotating angle of ~134° (Figures 2J and 2K). In addition to the RT's symmetry axis, a second 2-fold axis is observed at the *N*-glyco domains' interface of the caged effector dimer (Figures 2G and 2H).

Insights into the reverse transcription termination

Like its structural homologs, the RT catalytic site contains the typical palm, thumb, and fingers domains required for nucleic acid and nucleotide associations and catalysis (Figures S5E–S5H).[37] A comparison between the retron RT and two homologs[38,39] revealed an enzyme's post-catalytic state, in which the duplex between C73 and U82 and dA79 and dG85 of the msr-msDNA hybrid (i.e., the last nucleotides being transcribed) is accommodated in the catalytic groove (Figures S5E–S5I). The last incorporated nucleotide (dG85) is located near the catalytic residues (D197, D198, and D119), and its phosphate backbone is coordinated by Mg^{2+} and by D198 residues (Figure S5I). The mutation of the catalytic residues abrogated msDNA production and phage immunity, in line with previous observations[20–22,31] (Figures S5C and S5D).

Interestingly, U72, which is the next nucleotide to be transcribed, is flipped out probably due to a conformation of the msr-msDNA hybrid (Figure S5I). U72's base is stabilized by π-π stacking interactions with dA76 and dG77, thus preventing its entrance into the catalytic pocket. In addition, RTs use the fingers residues to coordinate the incoming nucleotide.[37] Retron-Eco1 fingers (R63 and K55) are ~9 Å away from the catalytic site and adopt an inactive state, as revealed by comparison with the group IIC intron[38] and Telomerase[39] RTs, representing active and inactive states, respectively (Figures S5E–S5K). Notably, the *msr* region 66–71, which connects the msr-msDNA duplex with the *msr* hairpins, likely displaces the β hairpin carrying the fingers in this state, preventing the coordination of the next incoming nucleotide (Figure S5L).

We designed mutants that include extra nucleotides after the *msr* nucleotide A66 (msr66+5poliA, msr66+10poliA, msr66+15-poliA) to test the role of the msr 66–71 region in reverse transcription termination. The mutants, including 5 or 10 additional nucleotides (msr66+5poliA, msr66+10poliA), produced longer msDNA products, supporting msr 66–71 region's role in reverse transcription termination (Figure S5C). Nevertheless, the three mutants also impacted the efficiency of msDNA production. These mutants abrogated the immunity against phages, which accounts for the combined action of their reduced msDNA production rates and the generation of longer msDNAs (Figure S5D).

The effector's dimerization is essential for assembly and defense

Both in the retron dimer structure[31] and the filament, the effector mainly interacts with the RT-msr-msDNA module through the helix-turn-helix (HTH) domain (Figure S6). Effector (R292A/R293A/K294A) and RT (R70A/A74R) mutants of residues involved in this interaction abrogated the anti-phage defense, in agreement with previous reports[31] (Figure S6B).

In the filament segments, the two antiparallel msDNA stem-loops interact with the positively charged surface of the effector and the final nucleotides of the *msr* (A80, C81, and U82), encapsulating an effector dimer (Figures 2G and 3A–3C). The effector dimerizes through the *N*-glyco domains and buries a wide interaction surface (~1,200 $Å^2$) in the segment's equator (Figure 3D). We mutated residues that establish key interactions in the dimerization interface (T105R, N112A, and Y137R) (Figures 3D–3F) and found that T105R abrogated filament assembly, producing particles like the retron dimer,[31] while Y137R and N112A formed shorter filaments than the WT (Figures 3G and S2G). The variety observed for the mutant filaments aligns well with the expected effects of the mutations, as T105 fits in a tight hydrophobic pocket where an arginine would clash with the second monomer, while Y137 is in a larger pocket that may fit a bulky side chain (Figure 3E). Conversely, N112 in one monomer associates with E84 in the other, and an alanine substitution could reduce the interaction affinity instead of entirely breaking it (Figure 3F).

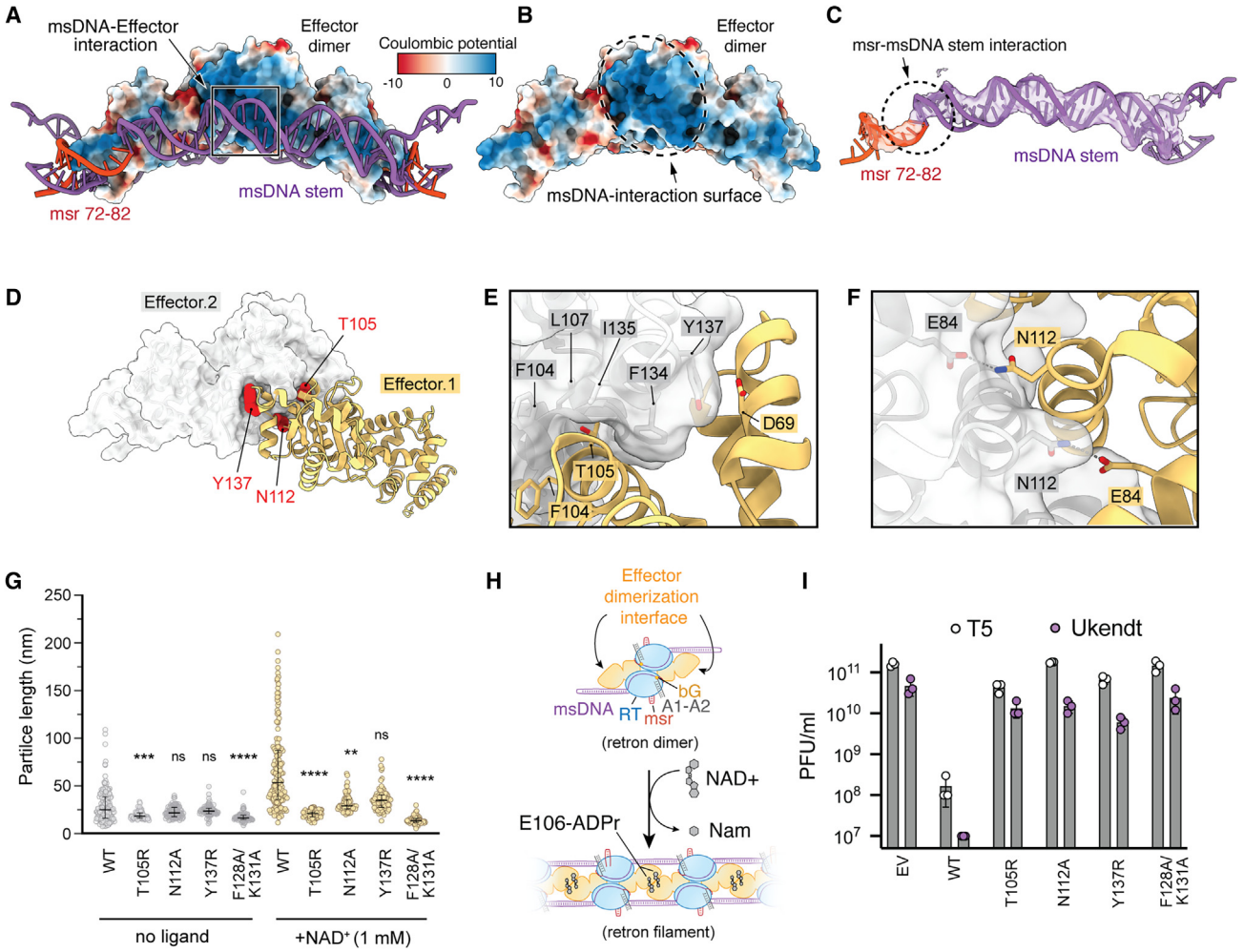

Figure 3. The Retron-Eco1 effector forms dimers in the filament

(A) Side view of the effector dimer and interactions with the msDNA. The msDNA and msr (72–82) are depicted as cartoons and the effector dimer as surface, colored according to the Coulombic potential.

(B) Surface representation of the effector, highlighting the positively charged msDNA-interaction surface.

(C) Cryo-EM map and model of msr (72–82) and the msDNA stem-loops and their interaction (dashed circle).

(D) Cartoon representation of the effector dimer. Effector.1 is depicted as a cartoon in wheat and Effector.2 as a transparent surface in gray. The residues involved in the dimerization (T105, N112, and Y137) are shown as balls in red.

(E) Close view of T105 and Y137's molecular environments.

(F) Close view of N112 and E84's molecular environment.

(G) Quantification of the maximum length of the particles observed with Retron-Eco1-WT and mutants incubated in the absence or presence of NAD^+ (1 mM) (see also Figure S2G). Data represent ~n = 70 particles and are plotted as the median ± interquartile range. Statistical analysis was performed by comparing each mutant with the corresponding WT (with and without ligand) using a Kruskal-Wallis test followed by Dunn's multiple comparison test. ns, non-significant, $^{**}p < 0.01$, $^{****}p < 0.0001$.

(H) Cartoon representation of the formation of Retron-Eco1 filaments by the assembly of retron dimers upon addition of NAD^+.

(I) Phage infection assay of *E. coli* MG1655 expressing Retron-Eco1-WT or its mutants. Plaque-forming units (PFUs) were quantified after infection with T5 (gray circles) and Ukendt phages (purple circles). Data are shown as the mean ± standard deviation (SD) of three biological replicates (n = 3).

Then, we exposed bacteria harboring Retron-Eco1-WT and the three mutants to Ukendt and T5 phages. The substitutions compromised the immune response, underscoring the relevance of filament assembly in immunity (Figures 3H and 3I).

ADPr is covalently bound to the catalytic residue

The effector dimer builds a pair of active pockets shared between the two monomers where additional densities were noted, indicating the presence of two ligands (Figures 4A and 4B). Local refinement of the segment region (Figures S3F and S3G; Table S2) allowed us to improve the map resolution to ~3.0 Å in this area. The density matched an ADPr moiety connected with the E106 side chain, supporting the presence of a covalent bond between the protein and the ligand (Figure 4B). To unveil the ligand's chemical nature, we performed a mass spectrometry (MS) analysis using electron-transfer/higher-energy collision

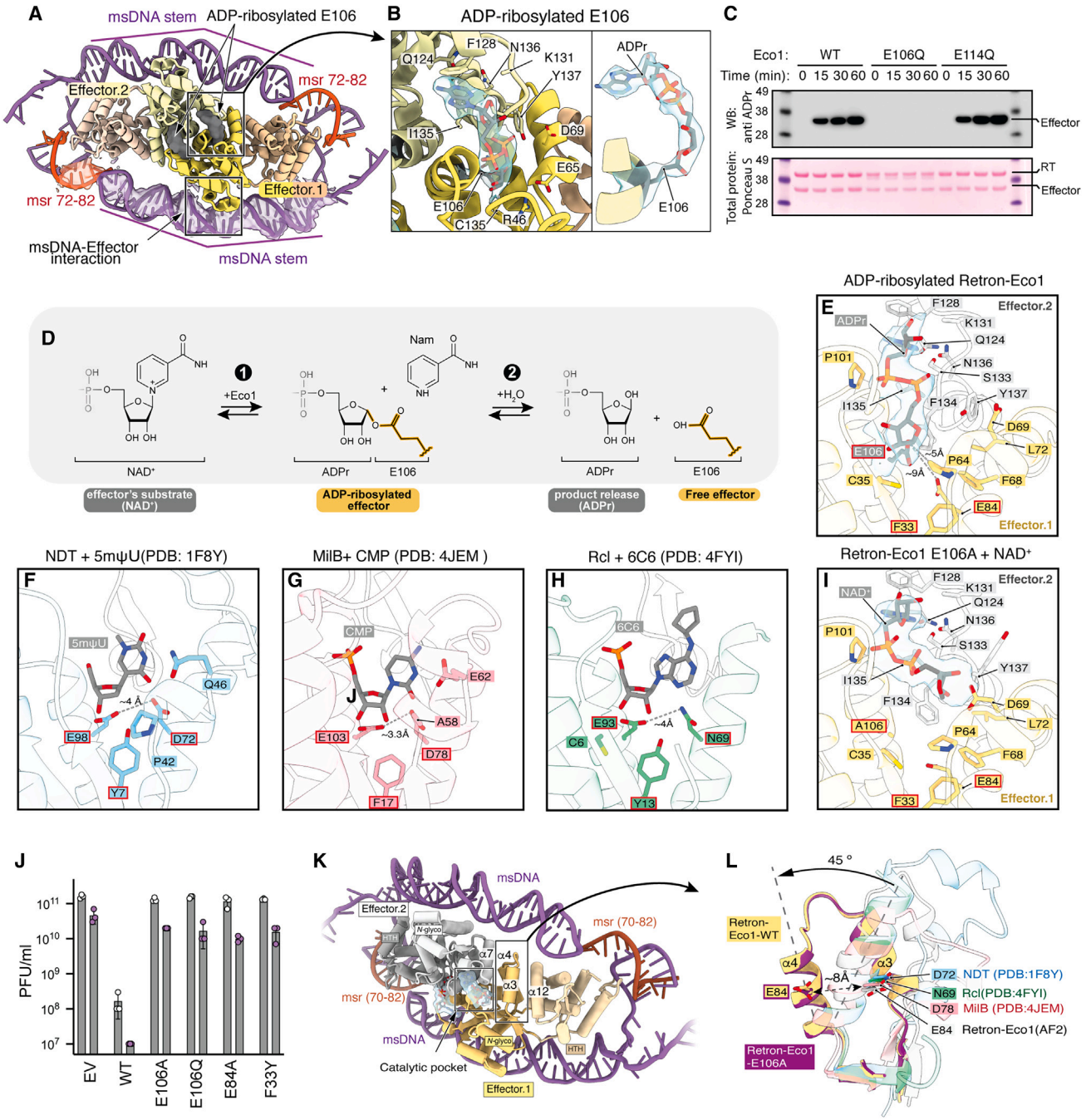

Figure 4. E106-ADPr represents a catalytic intermediate

(A) Cartoon representation of effector dimer surrounded by the msDNA stem-loops and msr (72–82). The ADPr molecules are shown as surface.

(B) Close view of the Retron-Eco1-effector catalytic pocket. The E106-ADPr cryo-EM is shown as a blue transparent surface.

(C) Detection of ADP-ribosylated effector by western blot using a specific ADPr antibody (see also Figure S7). The total amount of protein loaded in the gel was determined by staining the same membrane with Ponceau S. Representative experiment (n = 3 independent experiments).

(D) Schematic of the two-step NAD^+ hydrolysis reaction performed by Retron-Eco1. The formation of the E106-ADPr enzymatic intermediate and Nam release are depicted in the first step. The second step illustrates the hydrolysis of the ADP-ribosylated intermediate.

(E) Effector-WT catalytic site (EMDB: 18313, PDB: 8QBK) displaying the E106-ADPr linkage and residues important for ligand binding and catalysis as sticks. The E106-ADPr cryo-EM density is shown as a transparent surface.

(F) NDT catalytic site in complex with the non-cleavable substrate 5-methyl-2'-deuoxypsudouridine (PDB: 1F8Y).

(G) MilB catalytic site in complex with cytidine 5′-monophosphate (PDB: 4JEM).

(H) Rcl catalytic site in complex with 6-cyclopentyl-AMP (PDB: 4FYI).

(legend continued on next page)

dissociation (EThcD) fragmentation, which is uniquely capable of sequencing peptides while not perturbing the otherwise labile ADPr moiety[40] (STAR Methods). Our MS experiment allowed for nearly complete sequence coverage across the *N*-glyco effector (Figure S7A) and identified several ADP-ribosylation events that were highly induced upon NAD^+ addition (Table S3). Inspection of tandem mass spectrometry (MS/MS) spectra narrowed the localization of ADPr to an effector's small region (residues 106–117) and strongly suggested modification of E106 (86.3% localization probability) (Figures S7B–S7D). Treatment of the ADP-ribosylated effector with hydroxylamine, followed by detection with an ADPr antibody,[41] fully reverted the modification, supporting the ADPr-glutamate linkage[42,43] (Figure S7E). Although MS data suggested localization to E106, the nearby E114 was also a putative target. To investigate this possibility, we generated E106Q and E114Q mutants. Indeed, whereas the effector ADP-ribosylation was abolished with the E106Q mutant, no effect was observed for the E114Q mutation (Figure 4C). Hence, our combined analysis allowed the assignment of the extra density in the side chain of E106 to a covalently bound ADPr, one of the NAD^+ degradation products.

ADPr-E106 is an enzymatic intermediate

To comprehend the relationship between NAD^+ hydrolysis and filament assembly, we studied the effector ADP-ribosylation and the filament formation at different NAD^+ concentrations (Figures S7F–S7H). In the range of 100 μM to 1 mM NAD^+, which are typical NAD^+ concentrations in *E. coli* cytoplasm,[34,35] the *N*-glyco effector protein became ADP-ribosylated, leading to filament assembly (Figures S7F–S7H). This suggested that the filaments could be constitutively formed in the bacteria. Supporting this idea, we detected ADP-ribosylation of the effector in the bacteria after expression and before its isolation (Figure S7I). Next, we asked whether the effector was catalytically competent in the ADPr-linked form. To this end, we measured the activity of pre-ADP-ribosylated Retron-Eco1 filaments (STAR Methods). The pre-ADP-ribosylated Retron-Eco1 was able to hydrolyze the newly added NAD^+ at a slightly slower rate than the non-ADP-ribosylated Retron-Eco1 (~2 times slower) (Figures 1D and S7J; Table S1), corroborating that the enzyme is catalytically competent in the filament form. Further supporting this idea, Retron-Eco1 hydrolyzed a major part of the NAD^+ under substrate saturation conditions (Figure S7K).

Since the ADPr-linked E106 does not irreversibly inhibit NAD^+ hydrolysis, it could represent an enzymatic intermediate. Indeed, a comparison with the *N*-glyco's structural homologs (Figure 1C) revealed that the E106-ADPr linkage resembled the enzyme-(deoxy)-ribosyl catalytic intermediates reported in NDTs (Figure 4D),[44–48] which follow two-step "ping-pong" catalytic mechanisms. During the first step, the nucleotide base is released, and a covalent intermediate is formed between the catalytic glutamate side chain and C1′ of the (deoxy)ribosyl group, while another base or a water molecule acts as a nucleophile releasing the product in the second step.[49]

By comparing the effector active site with that of three NDT homologs[45,47,50] (Figures 4E–4I), we found a shared dimeric nature and arrangement of the catalytic residues. The Retron-Eco1 catalytic triad is formed by E106, F33, and E84 in one of the protomers (Effector.1) (Figures 4A, 4B, and 4E). These residues are conserved between type II-A1 and type II-A3 retrons but are variable in type II-A2 (Figures S8A and S8B), suggesting that the latter cannot cleave NAD^+ and thereby might play a different role or exert their toxicity through other mechanisms. The effector's E106 works as a nucleophile, which is ADP-ribosylated in the first part of the reaction, and mutation of this residue to A or Q abolishes phage protection (Figure 4J), consistent with previous observations.[20–22] On the other hand, F33 does not contact the ligand in the ADP-ribosylated state (Figure 4E). However, homologous residues in NDTs (Y7) and the cytidine 5′-monophosphate (CMP) hydrolase MilB (F17) are thought to discriminate between the presence and absence of an OH in the C2′ of the ribose, determining the specificity for ribose- or deoxyribose-containing substrates[50] (Figures 4F and 4G). A tyrosine substitution in this residue (F33Y) resulted in a complete loss of protection, supporting this notion (Figure 4J). The third putative catalytic residue E84 is functionally equivalent to D72, D78, and N69 in NDT, MilB, and the 5-hydroxymethyl-dUMP *N*-hydrolase Rcl (Figures 4A–4E) and seems to play a role by protonating the base-leaving group and activating the acceptor water molecule for the hydrolysis of the enzyme-(deoxy)ribosyl bond, as it has been proposed for MilB.[50] The substitution E84A also abrogated the retron-mediated immunity in line with the other catalytic mutants (Figure 4J).

On the opposite side of the catalytic pocket, the residues 128–140 from the second protomer coordinate the adenosine moiety and the two pyrophosphates of the ADPr (Figures 4A, 4B, 4E, 4I, and S8). Noteworthy, mutation of two of these residues (F128A/K131A) compromised filament assembly and anti-phage defense, underscoring the importance of the ligand binding (Figures 3G and S2G). These residues are conserved in type II-A3 retrons, but absent in the other structural homologs (NDT, MilB, and Rcl), suggesting their evolution in type II-A3 retron effectors to bind NAD^+ (Figures 4E–4I and S8).

The active site is in a catalytic inefficient configuration

The catalytic residue E84 is ~9 Å away from the E106-ADPr *O*-glycosidic bond (Figure 4E). E84's position is determined by a ~45° shift of the effector α3-α4 helical hairpin, compared with

(I) Effector-E106A catalytic site. NAD^+ cryo-EM density is shown as a transparent surface. The ADPr core of the NAD^+ molecule was built in the ligand's density.
(J) Phage infection assay of *E. coli* MG1655 expressing Retron-Eco1-WT or its mutants. Plaque-forming units (PFUs) were quantified after infection with T5 (gray circles) and Ukendt phages (purple circles). Data are shown as the mean ± standard deviation (SD) of three biological replicates (n = 3).
(K) Cartoon representation of the Retron-Eco1 effector dimer surrounded by the msDNA and msr (70–82). The positions of the helices α7, α12, and the helical hairpin α3-4 are marked.
(L) Comparison of the Retron-Eco1 α3-4 helical-hairpin position in the filamentous structures, and similar motifs in NDT, Rcl, MilB. The catalytic E84 and homologous residues are displayed as sticks. The Retron-Eco1-AF2 model is also depicted showing an "active" conformation. The main chains of the structures were superposed in coot with root-mean-square deviations (RMSDs) of ~4–5 Å over >100 residues.

that of other NDTs and is sandwiched by helix α12 of the same protomer and α7 of the second protomer (Figures 4K and 4L). In addition, E84 from one protomer hydrogen bonds with N112 from the other, further locking the residue's position (Figure 3F). This suggests that the Retron-Eco1 filament stabilizes the effector protein in a catalytically suboptimal state. In turn, the *N*-glyco domain opens the path to the catalytic site but exposes a group of hydrophobic residues (P64, F68, L72, L80, and F110), which likely protects the E106-ADPr *O*-glycosidic bond from hydrolysis (Figures 4E and 4I), as it has been proposed for NDTs[50] (Figure 4F). To visualize possible conformational changes in the active site, we performed a 3D classification of the segments (STAR Methods). This analysis showed that the segments undergo rotational movements in the knobs that are transmitted to the effector proteins sandwiched between the stem-loops of the msDNA (Video S1). However, the effector's α3-α4 helical hairpin remains locked despite these movements, suggesting that the filaments prevent the effector from adopting an active state. Collectively, these observations explain the filament's low NAD^+ hydrolysis activity (Figures 1D, 1F, S7J, and S7K) and the stabilization of the ADP-ribosylated E106 intermediate (Figure 4D). Additionally, the differences in the ADPr density might arise from the slow hydrolysis of the E106-ADPr covalent bond (Video S1).

The E106A mutant stabilizes a substrate-bound form

In the case of the E106A mutant, the catalytic site adopts a nearly identical configuration as the WT and presents density for a ligand that matches the ADPr moiety. However, the ligand's density does not support the presence of a covalent bond, as it cannot be formed with A106 (Figure 4I). We ascribed this density to the substrate of the reaction NAD^+, as inactivating mutations in other NAD^+-cleaving enzymes[51] or incubation with non-hydrolyzable NAD^+ analogs[18,52] typically yields substrate-bound structures by stabilizing pre-catalytic states. These findings explain the formation of long filaments observed in the Retron-Eco1-E106A mutant, as the bound NAD^+ cannot be hydrolyzed, thus stabilizing the assembly (Figures 2A, 2B, and S2A).

The msDNA prevents the effector's toxicity

Modification of msDNAs has been reported as a common line for the activation of retrons.[20,53] However, a mechanistic understanding of how msDNA alterations lead to retron-mediated toxicity is lacking. As the msDNA stem-loops encapsulate the effector dimer (Figure 4A), we speculated that they could stabilize the filament assembly (Video S1). To test this hypothesis, we designed two mutants that shortened the msDNA stem-loops by one (−1 turn) and two turns (−2 turn) of the DNA duplex. Expression of these mutants stalled bacterial growth (Figure 5A). However, this stark phenotype was reverted when they included the effector-inactivating E106A mutation, supporting that the growth defect arose from its *N*-glyco activity (Figure 5A).

Hence, we aimed to characterize the active mutants' structure. Attempts to purify the −2 turn mutant resulted in low yield due to its toxicity, limiting further characterization. On the other hand, we determined the structure of the −1 turn mutant (Figures S4E–S4J; Table S2). The mutant shared a similar architecture with Retron-Eco1-WT (Figures 5B, S3, and S4E–S4J). However, it displayed lower local resolution of the distal knob region in comparison with a more even distribution in the WT assembly (Figure S9A). Subsequent examination using OccuPy[54] verified the reduced map quality in these areas (Figure 5B) and estimated a comparable apparent occupancy (Figure S9B), thus implying the flexibility and misalignment of these components.[54]

We conducted 3D classification without alignment of the −1 turn mutant segments to resolve the conformational variation, which showed that ∼54% of the particles (class 2–5) produced maps of assembled segments (Figures S9C–S9E). However, they were more heterogeneous than the WT, with up to ∼20° rotation of the RT dimerization axis compared to ∼5° rotation in the WT filaments (Figure 5C). Despite these movements, we did not observe an active conformation of the α3-α4 helical hairpin in the maps. In turn, the remaining ∼46% of the particles (class 0–1) showed weaker density of the distal knob indicating higher conformational variation than the WT (Figures S9C and S9D). Additionally, ∼11% of the total particles produced a low-resolution map with poor density for the catalytic domain resembling the Retron-Eco1 dimer[31] (Figures S9F and S9G). Thus, this conformation likely represents disassembly stages in which the *N*-glyco domain is more flexible, probably allowing the conformational changes needed for effector activation. We also studied how msDNA shortening affects the morphology of the full filaments by negative staining. This analysis revealed that −1 turn mutant filaments are shorter than those of the WT (Figures 5D and 5E), further supporting the disassembly of the filaments (Figures 5B and 5C). Collectively, the msDNA stem-loops stabilize the filament architecture with the effector in a suboptimal activity state, while msDNA modifications promote the effector toxicity by the filaments' destabilization (Figure 5F).

Phages escape Retron-Eco1 immunity

Typically, phages develop immune resistance by acquiring mutations in the components that trigger immunity or by acquiring genes that inhibit or offset the immune effectors, thus offering clues about the system's mechanism of action.[55] To this end, we exposed *E. coli* cultures expressing Retron-Eco1 to infection by T5 or Ukendt phages and sought to select resistant mutants (Figure S10A; STAR Methods). In line with previous reports, we failed to isolate Retron-Eco1 escapers for T5, suggesting that the T5-encoded immune activator is crucial for phage survival.[53] In contrast, we obtained several Ukendt escapers (Figure S10B). Whole-genome sequencing of these retron-resistant phages, followed by comparative genomic analysis with the WT Ukendt genome, revealed mutations predominantly localized in two regions. One of them includes the gene *U69*, which presents mutations in three different forms: a frameshift mutation of the 8th codon, a start codon mutation, and a 3,357-bp region deletion. The other region, encompassing the genes *U54-U56*, was consistently duplicated across the Ukendt escaper mutants (Figure 6A). The pronounced toxicity of *U69* limited our functional characterization efforts of this protein. However, we observed that co-expression with Retron-Eco1 further intensified its toxic effect (Figure 6B), thereby suggesting that *U69* is involved in triggering the Retron-Eco1 Abi response. In addition, the highly basic character of U69 (Figure S10C; STAR Methods) aligns

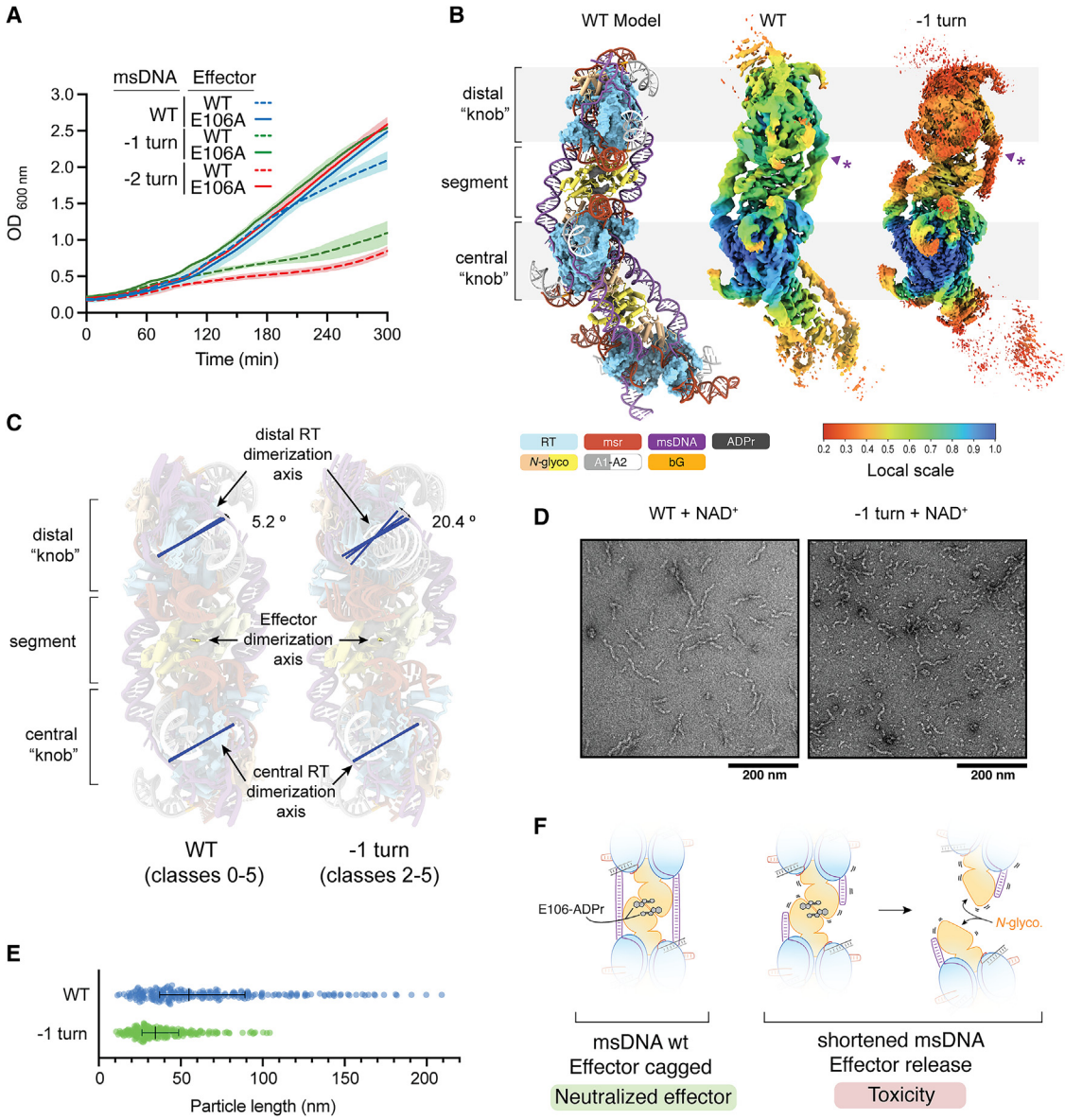

Figure 5. Shortening of the msDNA stem-loop causes toxicity

(A) Growth curves of *E. coli* MG1655(DE3) strain expressing different Retron-Eco1 msDNA mutants. The optical density at 600 nm ($OD_{600\ nm}$) was quantified over 300 min after expression. Data are shown as the mean ± standard deviation (SD) of three biological replicates (n = 3).

(B) Comparison between the consensus maps for Retron-Eco1-WT+ NAD^+ (EMDB: 19793) and −1 turn mutant + NAD^+ (EMDB: 19792). The local quality of the maps was calculated with OccuPy[54] and plotted on their surfaces (see also Figure S9).

(C) Comparison of the rotation of central and distal RT dimerization axes (blue lines) and the effector dimerization axis (yellow line) between Retron-Eco1-WT (classes 0–5) and the −1 turn mutant (classes 2–5). The axes were calculated in Chimera X by fitting the effector and RT dimers into the cryo-EM maps shown in Figures S9C and S9D.

(D) Representative negative staining micrographs of Retron-Eco1-WT and −1 turn mutant filaments upon NAD^+ incubation (1 mM). The scalebars represent 200 nm.

(E) Quantification of the filament lengths of the particles as shown in (D). Data shown for >n = 150 particles plotted as scatterplot with median ± interquartile range (SD).

(F) Cartoon representation of the filament's flexibility and disassembly induced by shortening the msDNA stem-loops, causing the release of the effector's *N*-glycosidase domain from the filament caging.

well with the DNA-interacting properties reported for all previously identified retron triggers[20] and is consistent with the proposed sensory role of the retron msDNA.

U56 is a phage-encoded Retron-Eco1 inhibitor

Then we explored the involvement of the duplicated *U54-U56* region in Ukendt's escaper phenotype. Previous studies have

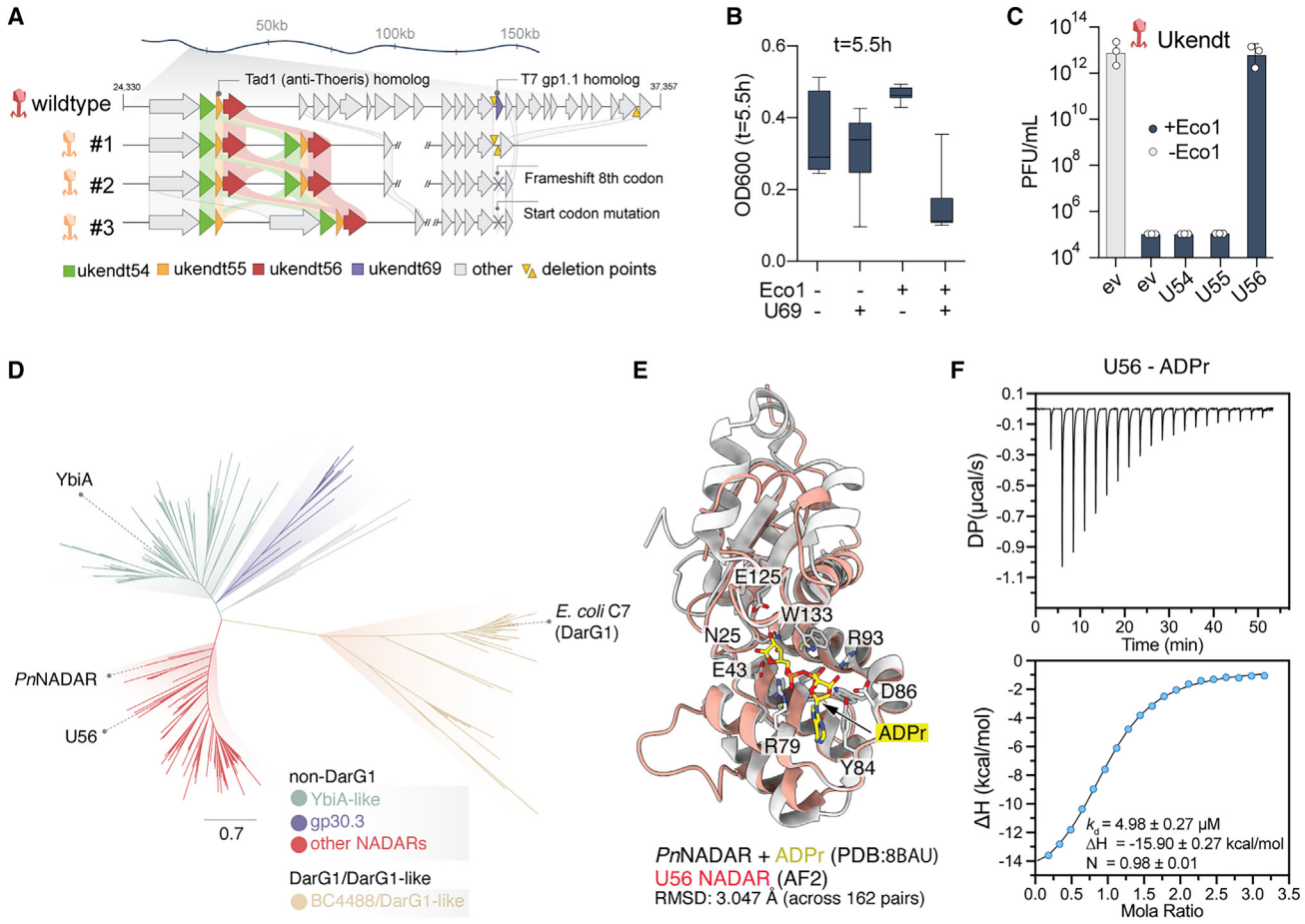

Figure 6. Phages evade Retron-Eco1 immune defense

(A) Overview of the mutations in the isolated escaper genomes, as detected by comparative genomics with the wild-type Ukendt genome (see also Figure S10).

(B) Toxicity testing of the phage-encoded Retron-Eco1 activator candidate U69 in the presence and absence of Eco1. Boxplots represent the OD600 after 5.5 h of growth. The data represent biological replicates (n = 12) plotted as the median ± interquartile range.

(C) Phage infection assay of *E. coli* MG1655 expressing Retron-Eco1-WT alone or in combination with the Ukendt U54–U56 proteins. Plaque-forming units (PFUs) were quantified after infection with T5 (gray circles) and Ukendt phages (purple circles). Data are shown as the mean ± standard deviation (SD) of three biological replicates (n = 3).

(D) Sequenced-based phylogenetic tree of the NADAR protein family. YbiA, *Pn*NADAR, *E. coli* C7 NADAR (DarG1), and U56 proteins are highlighted in the tree.

(E) Structural superposition of *Pn*NADAR with the U56 NADAR AlphaFold2 (AF2) model. The folding and the catalytic residues are conserved (RMSD: 3.047 Å across 162 atoms).

(F) Analysis of U56's binding to ADPr by ITC. U56, in a dimeric arrangement, binds ADPr in a 1:1 stoichiometry complex.

identified segmental amplifications in phage regions under defense system pressure, pinpointing the location of anti-phage defense genes.[56,57] Interestingly, sequence and structure-based analyses uncovered that one of the genes in this region (*U55*) encodes for a distant homolog of the anti-Thoeris defense protein Tad1,[58] further hinting at this region's putative anti-defense role (Figure S10D). To test this hypothesis, we independently expressed the three genes in the presence of Retron-Eco1 and subjected the cells to Ukendt infection. While *U54* and *U55* did not affect Retron-Eco1's anti-phage activity, *U56* completely abolished the defense phenotype (Figure 6C). These results revealed that *U56* functions as a phage-encoded inhibitor of Retron-Eco1 and are consistent with the emerging observation that anti-defense genes cluster in specific regions in mobile genetic elements, termed "anti-defense islands."[59,60]

We then focused on investigating the mechanism underlying *U56*'s antagonistic activity against Retron-Eco1. Sequence analyses revealed that U56 is a member of the extensive NAD^+ and ADPr (NADAR) family of proteins (Figure 6D). NADAR proteins are homologs of the bacterial YbiAs.[61] They are thought to interact with ADPr or ADPr-derived substrates and have been proposed to play a role in the regulation of the NAD^+ metabolism.[33,62] In addition, NADAR family members, DarG1 and the non-DarT-associated *Phytophthora nicotianae* var. parasitica NADAR (*Pn*NADAR), recently have been shown to hydrolyze the *N*-glycosidic bond between ADPr and guanosine bases generated by DarT1.[18] U56 clustered in a branch, including the non-DarT-associated

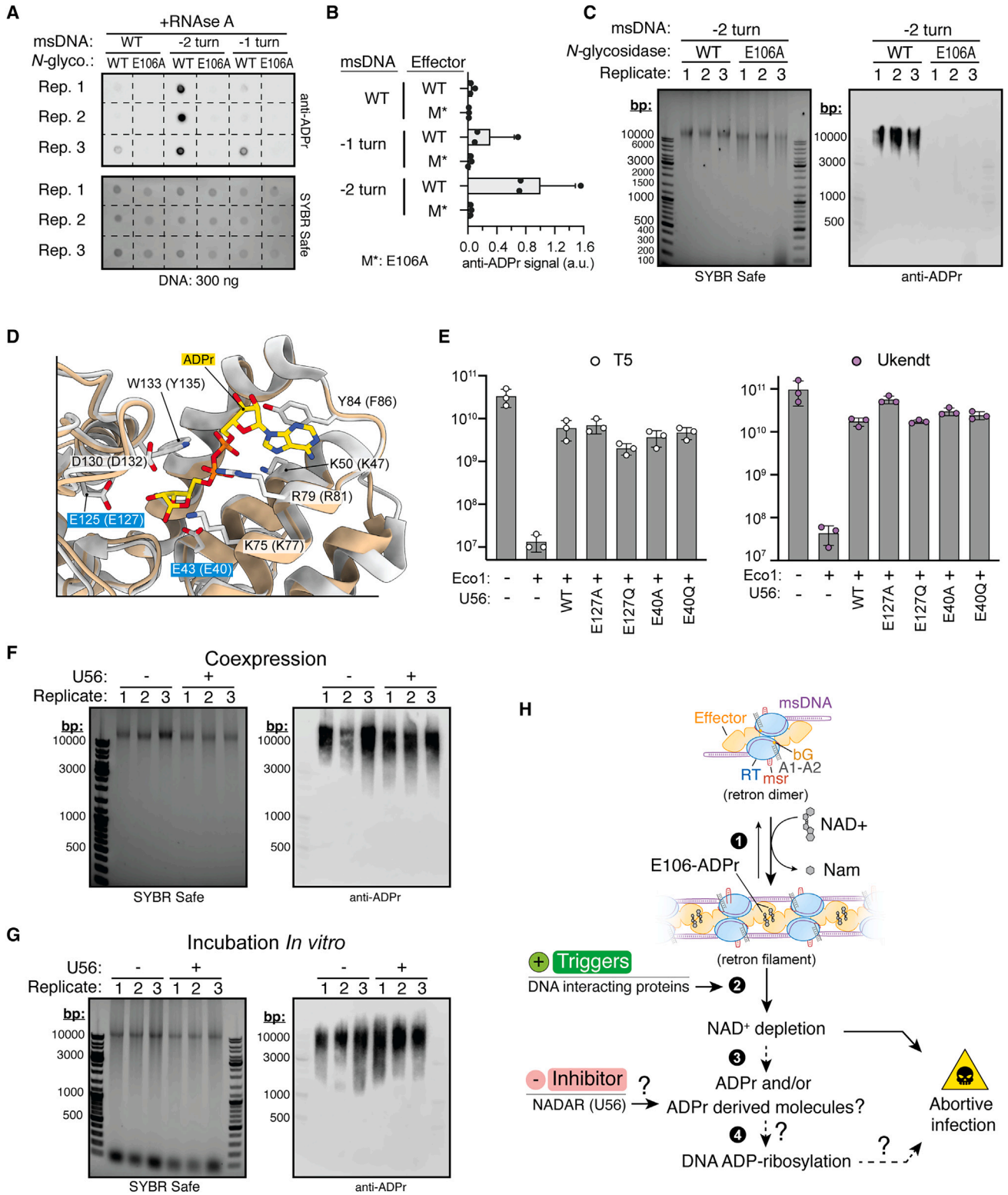

Figure 7. U56's catalytic activity is dispensable for inhibition

(A) Dot blot assay with anti-ADPr antibody showing the ADP-ribosylation of the total bacterial DNA upon expression of Retron-Eco1 toxic mutants.

(B) Quantification of the DNA ADP-ribosylation shown in (A), calculated as the ratio between the ADPr signal and the total DNA based on the densitometry of the dots. Data are shown as the mean ± standard deviation (SD) of three biological replicates (n = 3) (see also Figure S10).

(legend continued on next page)

NADARs (e.g., *Pn*NADAR). To gain insights into U56's function, we generated a U56 model using AlphaFold2[63] and performed a structural superposition with *Pn*NADAR in complex with ADPr. This analysis revealed that the predicted folding and the catalytic residues are conserved between U56 and *Pn*NADAR (Figures 6E, S10E, and S10F). Then, we tested U56's ability to bind ADPr. Isothermal titration calorimetry (ITC) confirmed that U56 binds ADPr in a dimeric arrangement with a dissociation constant (k_d) of ~5 μM (Figure 6F).

The retron activity leads to DNA ADP-ribosylation

Our findings indicating that Retron-Eco1 does not produce soluble ADPr following phage infection (Figure 1H), combined with U56's inhibitory effect on Retron-Eco1 and its similarity to ADP-ribosyl hydrolases (DarG1), led us to hypothesize that the ADPr generated by the effector might be transferred to the DNA, akin to the way DarT1 induces toxicity.[18] To explore this hypothesis, we expressed Retron-Eco1-WT along with the toxic mutants (−1 turn and −2 turn), purified the total DNA, and then conducted immunoblot analysis using an ADPr antibody[41] (Figures 7A and 7B; STAR Methods). The level of ADPr on the sample was almost undetectable when Retron-Eco1-WT was expressed. Conversely, the mutants produced a stronger ADPr signal, especially the one with the shorter stem-loop (−2 turn) (Figures 7A and 7B). We further characterized the DNA-ADP-ribosylation by size-resolving the sample's components by electrophoresis, which attributed the ADPr signal to the DNA (>10,000 nt) (Figure 7C). Noteworthy, the combination of these mutants with the effector E106A inactivating mutation yielded an almost undetectable ADP-ribosylation signal, supporting the relevance of the effector catalytic activity for DNA modification (Figures 7A–7C).

Then, we asked if the retron can ADP-ribosylate DNA directly. To address this question, we incubated the recombinant −1 turn mutant with eight oligonucleotides of different sequences (STAR Methods; Table S4) and monitored the oligonucleotide's migration using denaturing electrophoresis. No DNA's shifts were observed in this experiment (Figure S10G), supporting that Retron-Eco1 does not ADP-ribosylate DNA under these conditions. Although the experiments cannot rule out the possibility of the direct transfer of the ADPr to DNA by Retron-Eco1 (e.g., if the target site is sequence- or shape-specific), they suggest the requirement of an intermediate factor. This notion is also supported by the lack of structural homology between the Retron-Eco1 effector and other DNA-modifying ARTs.[15,17,18,64]

U56's possible hydrolytic activity is dispensable for inhibition

Finally, we tested if U56's possible hydrolytic activity is essential for Retron-Eco1 inhibition, in a similar fashion as DarG1 and NADAR enzymes inhibit DarT1 toxin by cleaving the ADPr-guanosine *N*-glycosidic bond.[18] To this end, we mutated the putative catalytic residues (E127 and E40) identified by comparison with *Phytophthora nicotianae* var. parasitica NADAR (E125 and E43) (Figures 7D and S10E), and we tested their phenotype during phage infection. U56's catalytic mutants still neutralized Retron-Eco1 immunity, supporting the notion that its possible hydrolytic activity is dispensable for the inhibition (Figure 7E). Consistent with this concept, co-expressing U56 with Retron-Eco1 or treating ADP-ribosylated DNA, produced by expressing the −2 turn mutant with U56 *in vitro* (Figures 7F and 7G), did not reverse the ADP-ribosylation on the DNA. Collectively, this suggests that U56's inhibitory mechanism differs from DarG1 and does not involve hydrolyzing the ADPr from the DNA.

DISCUSSION

In this study, we have dissected the singular anti-phage defense mechanism of Retron-Eco1. The activity of Retron-Eco1 requires the formation of filaments that build the shared catalytic sites at the dimerization interface of the *N*-glyco domains. Therefore, this suggests that the Retron-Eco1 dimer[31] cannot undergo NAD^+ cleavage, owing to the catalytic sites being unassembled (Figure 7H). In turn, the dimeric form constitutes the building block of the filaments that are assembled at typical bacterial cytosolic NAD^+ concentrations.[34,35] In the absence of phage infection, the suboptimal activity of the non-activated effector induces the filamentous assembly (Figure 7H). Furthermore, we observe ADP-ribosylation of the Retron-Eco1 effector inside the bacteria before purification, supporting that Retron-Eco1 should form filaments *in situ* (Figure S7I). Retron-Eco1 filaments cage the effector protein in a low-activity state; however, they are loaded with ADPr that is poised for release (Figure 7H). Within this framework, a prepared immune state would enable a swift and enhanced response to minimal signs of infection. Moreover, the requirement of higher-order assemblies for activity may

(C) Confirmation of the bacterial DNA ADP-ribosylation. The samples from (A) were size-resolved by electrophoresis and transferred to a nylon membrane, followed by detection with an anti-ADPr antibody. Data are shown for n = 3 biological replicates.
(D) Catalytic pocket of the *Pn*NADAR in complex with ADPr, in gray (PDB: 8BAU), superposed with U56 AlphaFold2 model, in wheat (RMSD: 3.047 Å across 162 atoms). ADPr and *Pn*NADAR residues coordinating the ADPr are displayed as sticks. E125 and E43 catalytic residues are framed in a blue box. U56's homologous residues are shown in parenthesis.
(E) Phage infection assay of *E. coli* MG1655 expressing Retron-Eco1-WT alone or in combination with the Ukendt U56-WT and mutants. Plaque-forming units (PFUs) were quantified after infection with T5 (gray circles) and Ukendt phages (purple circles). Data are shown as the mean ± standard deviation (SD) of three biological replicates (n = 3).
(F) Effect of U56 expression with Retron-Eco1 on the ADP-ribosylation of DNA.
(G) In vitro hydrolase experiment. ADP-ribosylated DNA was incubated with U56. Data are shown as the mean ± standard deviation (SD) of three biological replicates (n = 3) in (F) and (G).
(H) Proposed model of Retron-Eco1 immune mechanism. (1) Retron-Eco1 is in an equilibrium between dimeric and filament forms. The filaments are in an "armed" state, by stalling the catalytic reaction in an intermediate state where ADPr is linked to E106. (2) Retron triggers (i.e., DNA-interacting proteins) would initiate the continuation of the enzymatic reaction and the release of the ADPr. This would cause NAD^+ depletion and the transfer of ADPr to the bacterial DNA by unknown mechanisms (3–4) (dashed lines).

serve as a safeguard mechanism to prevent autoimmunity by the accidental production of highly cytotoxic effectors. On a wider scale, the formation of Retron-Eco1 filaments is consistent with the emerging observation of the oligomerization of immune components in cellular antiviral responses.[14,65,66]

The molecular events underpinning Retron-Eco1 activation during phage infection have remained enigmatic. In this regard, several DNA-interacting proteins have been recently described to trigger different retrons, supporting a sensory role of the msDNA in their activation.[20,53] This is consistent with our phage escape analysis where we identified a potential activator (*U69*), coding for a small protein predicted to interact with DNA, which could not be further characterized because of its intrinsic toxicity. To better understand the msDNA-mediated regulation of the retron activity, we engineered the msDNA mutants. The structural analysis showed that the filaments formed by the mutant are less stable, facilitating the effector release from the filament and promoting toxicity (Figure 5). Based on this, we speculate that natural triggers could induce similar processes leading to Abi.

Retron-Eco1 leads to NAD^+ depletion (Figure 1G), which will likely impact both bacterial and phage metabolism by reducing the levels of this key metabolite.[67] Supporting this idea, the low NAD^+ concentrations detected at longer infection times (<80 μM) are thought to have a bacteriostatic effect.[35] Additionally, we discovered that the msDNA mutants cause DNA ADP-ribosylation (Figures 7A–7C). Noteworthy, ADP-ribosylation activates the DNA damage response in bacteria, possibly interfering with replication and transcription,[19] thereby hinting at a potential role in retron toxicity. We also identified a phage-encoded Retron-Eco1 inhibitor (*U56*), which encodes a NADAR protein, whose possible hydrolytic activity is dispensable for Retron-Eco1 inhibition (Figures 7E–7G). While the exact molecular mechanisms by which U56 inhibits Retron-Eco1 are still unclear, the data indicate that it would likely involve binding to soluble ADPr or its derivatives. This is consistent with the recent identification of numerous phage-encoded inhibitors that sequester small molecules to bypass host defenses.[58,68–70]

Collectively, our study broadens our mechanistic understanding of bacteria-phage interactions, drawing parallels with eukaryotic innate immunity.[71] With the increase in antibiotic-resistant bacteria, there's a pressing need for alternative antimicrobial approaches such as phage therapy, which necessitates a deeper understanding of these interactions. Thus, our findings will likely contribute to the development of new molecular tools to combat pathogenic bacteria.

Limitations of the study

Our data support the formation of the Retron-Eco1 filaments in bacteria. However, the observation of the filaments *in situ* remains unexplored. Further research is also needed to understand the activation of Retron-Eco1 by the natural triggers, and the effects of NAD^+ depletion on bacterial and/or phage metabolism during infection. Further research is necessary to delve into the observed DNA ADP-ribosylation, focusing on identifying potential ARTs responsible for ADPr transfer to DNA, pinpointing ADPr targets within the DNA, and understanding how phage and/or host DNA ADP-ribosylation influences retron immunity. Although U56 binds to ADPr, additional studies are required to fully comprehend how U56 bypasses retron immunity, as well as to explore the capability of U56 and other NADAR proteins as inhibitors of other NAD^+/ADPr-associated immune systems.

STAR★METHODS

Detailed methods are provided in the online version of this paper and include the following:

- KEY RESOURCES TABLE
- RESOURCE AVAILABILITY
  - Lead contact
  - Materials availability
  - Data and code availability
- EXPERIMENTAL MODEL AND STUDY PARTICIPANT DETAILS
  - Microbe strains
- METHOD DETAILS
  - DNA and molecular biology
  - Phage infection assays
  - Phage and protein trees and comparisons
  - Protein expression and purification
  - *In vitro* NAD^+ cleavage assays
  - Bacterial metabolites detection by LC-MS
  - Structural biology
  - Detection of ADP-ribosylated proteins
  - Growth curves with msDNA mutants
  - Phage escaper analysis
  - Isothermal titration calorimetry
  - DNA ADP-ribosylation
- QUANTIFICATION AND STATISTICAL ANALYSIS

SUPPLEMENTAL INFORMATION

Supplemental information can be found online at https://doi.org/10.1016/j.molcel.2024.05.001.

ACKNOWLEDGMENTS

We thank the Danish cryo-EM National Facility in CFIM (University of Copenhagen) and Nicholas Sofos for cryo-EM data collection support. We thank Raissa Novais, Mansa Nair-Kihara, and Thomas Moritz (Novo Nordisk Foundation Center for Basic Metabolic Research, University of Copenhagen) for their help in preliminary metabolomic experiments. We acknowledge Feng Zhang (Broad Institute and MIT, Cambridge) for kindly providing pLG001 and pLG007 plasmids (Addgene plasmids #157879 and #157885). We thank Lars Hansen and Nikoline S. Olsen (Department of Plant and Environmental Sciences, PLEN, University of Copenhagen), Jakob Bobonis (Typas group, EMBL), and Claudia Igler (ETH, Zurich) for kindly providing the coliphages used here. We thank Søren J. Sørensen for generously granting us access to the laboratory space and technical equipment at the Section of Microbiology (University of Copenhagen). This work was supported by Lundbeck Foundation grants R347-2020-2346 and R380-2021-1448 awarded to R.P.-R. and A.C., respectively. G.M. and M.L.N. are part of the Novo Nordisk Foundation Center for Protein Research (NNF-CPR), which is supported financially by the Novo Nordisk Foundation (grant NNF14CC0001). M.L.N. is also supported by The Danish Council of Independent Research (0135-00096B, 2034-00311B, and 2032-00311B), The Danish Cancer Society (R146-A9159-16-S2), and the European Union's Horizon 2020 research and innovation program under grant agreement EPIC-XS-823839. This work was also supported by the NNF0024386, NNF17SA0030214, Distinguished Investigator NNF18OC0055061, Distinguished Innovator NNF23OC0082600, and ERC_AdG_101096548 INTETOOLS grants to G.M. who is a member of the Integrative Structural Biology Cluster (ISBUC) at the University of Copenhagen.

AUTHOR CONTRIBUTIONS

Conceptualization, A.C., S.C.-W., M.R.M., R.P.-R., and G.M.; methodology, A.C., S.C.-W., M.R.M., B.L.-M., and I.A.H.; software, M.R.M.; investigation, A.C., S.C.-W., M.R.M., B.L.-M., I.A.H., R.Z., T.P., A.F., and S.H.-C.L.; resources, G.M. and M.L.N.; data curation, A.C., M.R.M., B.L.-M., and I.A.H.; writing – original draft, A.C., R.P.-R., and G.M.; writing – review & editing, A.C., R.P.-R., and G.M.; visualization, A.C., S.C.-W., M.R.M., B.L.-M., and I.A.H.; supervision, A.C., R.P.-R., M.L.N., and G.M.; project administration, A.C., R.P.-R., M.L.N., and G.M.; funding acquisition, A.C., R.P.-R., M.L.N., and G.M.

DECLARATION OF INTERESTS

G.M. is a stockholder and member of the SAB of Ensoma, and M.R.M. is listed as co-inventor of patent application WO2023141602A2, related to the use of engineered retrons for genome editing.

Received: September 26, 2023
Revised: March 15, 2024
Accepted: May 1, 2024
Published: May 23, 2024

REFERENCES

1. Bernheim, A., Millman, A., Ofir, G., Meitav, G., Avraham, C., Shomar, H., Rosenberg, M.M., Tal, N., Melamed, S., Amitai, G., and Sorek, R. (2021). Prokaryotic viperins produce diverse antiviral molecules. Nature *589*, 120–124. https://doi.org/10.1038/s41586-020-2762-2.
2. Kronheim, S., Daniel-Ivad, M., Duan, Z., Hwang, S., Wong, A.I., Mantel, I., Nodwell, J.R., and Maxwell, K.L. (2018). A chemical defence against phage infection. Nature *564*, 283–286. https://doi.org/10.1038/s41586-018-0767-x.
3. Georjon, H., and Bernheim, A. (2023). The highly diverse antiphage defence systems of bacteria. Nat. Rev. Microbiol. *21*, 686–700. https://doi.org/10.1038/s41579-023-00934-x.
4. Mayo-Muñoz, D., Pinilla-Redondo, R., Birkholz, N., and Fineran, P.C. (2023). A host of armor: prokaryotic immune strategies against mobile genetic elements. Cell Rep. *42*, 112672. https://doi.org/10.1016/j.celrep.2023.112672.
5. Tock, M.R., and Dryden, D.T.F. (2005). The biology of restriction and anti-restriction. Curr. Opin. Microbiol. *8*, 466–472. https://doi.org/10.1016/j.mib.2005.06.003.
6. Nussenzweig, P.M., and Marraffini, L.A. (2020). Molecular mechanisms of CRISPR-Cas immunity in bacteria. Annu. Rev. Genet. *54*, 93–120. https://doi.org/10.1146/annurev-genet-022120-112523.
7. Lopatina, A., Tal, N., and Sorek, R. (2020). Abortive infection: bacterial suicide as an antiviral immune strategy. Annu. Rev. Virol. *7*, 371–384. https://doi.org/10.1146/annurev-virology-011620-040628.
8. Ofir, G., Herbst, E., Baroz, M., Cohen, D., Millman, A., Doron, S., Tal, N., Malheiro, D.B.A., Malitsky, S., Amitai, G., and Sorek, R. (2021). Antiviral activity of bacterial TIR domains via immune signalling molecules. Nature *600*, 116–120. https://doi.org/10.1038/s41586-021-04098-7.
9. Tamulaitiene, G., Sabonis, D., Sasnauskas, G., Ruksenaite, A., Silanskas, A., Avraham, C., Ofir, G., Sorek, R., Zaremba, M., and Siksnys, V. (2024). Activation of Thoeris antiviral system via SIR2 effector filament assembly. Nature *627*, 431–436. https://doi.org/10.1038/s41586-024-07092-x.
10. Morehouse, B.R., Govande, A.A., Millman, A., Keszei, A.F.A., Lowey, B., Ofir, G., Shao, S., Sorek, R., and Kranzusch, P.J. (2020). STING cyclic dinucleotide sensing originated in bacteria. Nature *586*, 429–433. https://doi.org/10.1038/s41586-020-2719-5.
11. Tal, N., Morehouse, B.R., Millman, A., Stokar-Avihail, A., Avraham, C., Fedorenko, T., Yirmiya, E., Herbst, E., Brandis, A., Mehlman, T., et al. (2021). Cyclic CMP and cyclic UMP mediate bacterial immunity against phages. Cell *184*, 5728–5739.e16. https://doi.org/10.1016/j.cell.2021.09.031.
12. Koopal, B., Potocnik, A., Mutte, S.K., Aparicio-Maldonado, C., Lindhoud, S., Vervoort, J.J.M., Brouns, S.J.J., and Swarts, D.C. (2022). Short prokaryotic Argonaute systems trigger cell death upon detection of invading DNA. Cell *185*, 1471–1486.e19. https://doi.org/10.1016/j.cell.2022.03.012.
13. Garb, J., Lopatina, A., Bernheim, A., Zaremba, M., Siksnys, V., Melamed, S., Leavitt, A., Millman, A., Amitai, G., and Sorek, R. (2022). Multiple phage resistance systems inhibit infection via SIR2-dependent NAD(+) depletion. Nat. Microbiol. *7*, 1849–1856. https://doi.org/10.1038/s41564-022-01207-8.
14. Kagan, J.C., Magupalli, V.G., and Wu, H. (2014). SMOCs: supramolecular organizing centres that control innate immunity. Nat. Rev. Immunol. *14*, 821–826. https://doi.org/10.1038/nri3757.
15. Mikolčević, P., Hloušek-Kasun, A., Ahel, I., and Mikoč, A. (2021). ADP-ribosylation systems in bacteria and viruses. Comp. Struct. Biotechnol. J. *19*, 2366–2383. https://doi.org/10.1016/j.csbj.2021.04.023.
16. LeRoux, M., Srikant, S., Teodoro, G.I.C., Zhang, T., Littlehale, M.L., Doron, S., Badiee, M., Leung, A.K.L., Sorek, R., and Laub, M.T. (2022). The DarTG toxin-antitoxin system provides phage defence by ADP-ribosylating viral DNA. Nat. Microbiol. *7*, 1028–1040. https://doi.org/10.1038/s41564-022-01153-5.
17. Schuller, M., Butler, R.E., Ariza, A., Tromans-Coia, C., Jankevicius, G., Claridge, T.D.W., Kendall, S.L., Goh, S., Stewart, G.R., and Ahel, I. (2021). Molecular basis for DarT ADP-ribosylation of a DNA base. Nature *596*, 597–602. https://doi.org/10.1038/s41586-021-03825-4.
18. Schuller, M., Raggiaschi, R., Mikolcevic, P., Rack, J.G.M., Ariza, A., Zhang, Y., Ledermann, R., Tang, C., Mikoc, A., and Ahel, I. (2023). Molecular basis for the reversible ADP-ribosylation of guanosine bases. Mol. Cell *83*, 2303–2315.e6. https://doi.org/10.1016/j.molcel.2023.06.013.
19. Lawarée, E., Jankevicius, G., Cooper, C., Ahel, I., Uphoff, S., and Tang, C.M. (2020). DNA ADP-ribosylation stalls replication and is reversed by RecF-mediated homologous recombination and nucleotide excision repair. Cell Rep. *30*, 1373–1384.e4. https://doi.org/10.1016/j.celrep.2020.01.014.
20. Bobonis, J., Mitosch, K., Mateus, A., Karcher, N., Kritikos, G., Selkrig, J., Zietek, M., Monzon, V., Pfalz, B., Garcia-Santamarina, S., et al. (2022). Bacterial retrons encode phage-defending tripartite toxin-antitoxin systems. Nature *609*, 144–150. https://doi.org/10.1038/s41586-022-05091-4.
21. Millman, A., Bernheim, A., Stokar-Avihail, A., Fedorenko, T., Voichek, M., Leavitt, A., Oppenheimer-Shaanan, Y., and Sorek, R. (2020). Bacterial retrons function in anti-phage defense. Cell *183*, 1551–1561.e12. https://doi.org/10.1016/j.cell.2020.09.065.
22. Gao, L., Altae-Tran, H., Böhning, F., Makarova, K.S., Segel, M., Schmid-Burgk, J.L., Koob, J., Wolf, Y.I., Koonin, E.V., and Zhang, F. (2020). Diverse enzymatic activities mediate antiviral immunity in prokaryotes. Science *369*, 1077–1084. https://doi.org/10.1126/science.aba0372.
23. Mestre, M.R., González-Delgado, A., Gutiérrez-Rus, L.I., Martínez-Abarca, F., and Toro, N. (2020). Systematic prediction of genes functionally associated with bacterial retrons and classification of the encoded tripartite systems. Nucleic Acids Res. *48*, 12632–12647. https://doi.org/10.1093/nar/gkaa1149.
24. Yee, T., Furuichi, T., Inouye, S., and Inouye, M. (1984). Multicopy single-stranded DNA isolated from a gram-negative bacterium, Myxococcus xanthus. Cell *38*, 203–209. https://doi.org/10.1016/0092-8674(84)90541-5.
25. Bhattarai-Kline, S., Lear, S.K., Fishman, C.B., Lopez, S.C., Lockshin, E.R., Schubert, M.G., Nivala, J., Church, G.M., and Shipman, S.L. (2022). Recording gene expression order in DNA by CRISPR addition of retron

barcodes. Nature *608*, 217–225. https://doi.org/10.1038/s41586-022-04994-6.

26. Kong, X., Wang, Z., Zhang, R., Wang, X., Zhou, Y., Shi, L., and Yang, H. (2021). Precise genome editing without exogenous donor DNA via retron editing system in human cells. Protein Cell *12*, 899–902. https://doi.org/10.1007/s13238-021-00862-7.
27. Simon, A.J., Ellington, A.D., and Finkelstein, I.J. (2019). Retrons and their applications in genome engineering. Nucleic Acids Res. *47*, 11007–11019. https://doi.org/10.1093/nar/gkz865.
28. Lopez, S.C., Crawford, K.D., Lear, S.K., Bhattarai-Kline, S., and Shipman, S.L. (2022). Precise genome editing across kingdoms of life using retron-derived DNA. Nat. Chem. Biol. *18*, 199–206. https://doi.org/10.1038/s41589-021-00927-y.
29. Dhundale, A., Lampson, B., Furuichi, T., Inouye, M., and Inouye, S. (1987). Structure of msDNA from Myxococcus xanthus: evidence for a long, self-annealing RNA precursor for the covalently linked, branched RNA. Cell *51*, 1105–1112. https://doi.org/10.1016/0092-8674(87)90596-4.
30. Palka, C., Fishman, C.B., Bhattarai-Kline, S., Myers, S.A., and Shipman, S.L. (2022). Retron reverse transcriptase termination and phage defense are dependent on host RNase H1. Nucleic Acids Res. *50*, 3490–3504. https://doi.org/10.1093/nar/gkac177.
31. Wang, Y., Guan, Z., Wang, C., Nie, Y., Chen, Y., Qian, Z., Cui, Y., Xu, H., Wang, Q., Zhao, F., et al. (2022). Cryo-EM structures of Escherichia coli Ec86 retron complexes reveal architecture and defence mechanism. Nat. Microbiol. *7*, 1480–1489. https://doi.org/10.1038/s41564-022-01197-7.
32. Olsen, N.S., Forero-Junco, L., Kot, W., and Hansen, L.H. (2020). Exploring the remarkable diversity of culturable Escherichia coli phages in the Danish wastewater environment. Viruses *12*, 986. https://doi.org/10.3390/v12090986.
33. Iyer, L.M., Burroughs, A.M., Anantharaman, V., and Aravind, L. (2022). Apprehending the NAD(+)-ADPr-dependent systems in the virus world. Viruses *14*, 1977. https://doi.org/10.3390/v14091977.
34. Santos, A.R.S., Gerhardt, E.C.M., Parize, E., Pedrosa, F.O., Steffens, M.B.R., Chubatsu, L.S., Souza, E.M., Passaglia, L.M.P., Sant'Anna, F.H., de Souza, G.A., et al. (2020). NAD(+) biosynthesis in bacteria is controlled by global carbon/nitrogen levels via PII signaling. J. Biol. Chem. *295*, 6165–6176. https://doi.org/10.1074/jbc.RA120.012793.
35. Zhou, Y., Wang, L., Yang, F., Lin, X., Zhang, S., and Zhao, Z.K. (2011). Determining the extremes of the cellular NAD(H) level by using an Escherichia coli NAD(+)-auxotrophic mutant. Appl. Environ. Microbiol. *77*, 6133–6140. https://doi.org/10.1128/AEM.00630-11.
36. Ka, D., Oh, H., Park, E., Kim, J.H., and Bae, E. (2020). Structural and functional evidence of bacterial antiphage protection by Thoeris defense system via NAD(+) degradation. Nat. Commun. *11*, 2816. https://doi.org/10.1038/s41467-020-16703-w.
37. Joyce, C.M., and Steitz, T.A. (1994). Function and structure relationships in DNA polymerases. Annu. Rev. Biochem. *63*, 777–822. https://doi.org/10.1146/annurev.bi.63.070194.004021.
38. Stamos, J.L., Lentzsch, A.M., and Lambowitz, A.M. (2017). Structure of a thermostable Group II intron reverse transcriptase with template-primer and its functional and evolutionary implications. Mol. Cell *68*, 926–939.e4. https://doi.org/10.1016/j.molcel.2017.10.024.
39. Mitchell, M., Gillis, A., Futahashi, M., Fujiwara, H., and Skordalakes, E. (2010). Structural basis for telomerase catalytic subunit TERT binding to RNA template and telomeric DNA. Nat. Struct. Mol. Biol. *17*, 513–518. https://doi.org/10.1038/nsmb.1777.
40. Hendriks, I.A., Larsen, S.C., and Nielsen, M.L. (2019). An advanced strategy for comprehensive profiling of ADP-ribosylation sites using mass spectrometry-based proteomics. Mol. Cell. Proteomics *18*, 1010–1026. https://doi.org/10.1074/mcp.TIR119.001315.
41. Hendriks, I.A., Buch-Larsen, S.C., Prokhorova, E., Elsborg, J.D., Rebak, A.K.L.F.S., Zhu, K., Ahel, D., Lukas, C., Ahel, I., and Nielsen, M.L. (2021). The regulatory landscape of the human HPF1- and ARH3-dependent ADP-ribosylome. Nat. Commun. *12*, 5893. https://doi.org/10.1038/s41467-021-26172-4.
42. Moss, J., Yost, D.A., and Stanley, S.J. (1983). Amino acid-specific ADP-ribosylation. J. Biol. Chem. *258*, 6466–6470. https://doi.org/10.1016/S0021-9258(18)32434-7.
43. Palazzo, L., Leidecker, O., Prokhorova, E., Dauben, H., Matic, I., and Ahel, I. (2018). Serine is the major residue for ADP-ribosylation upon DNA damage. eLife *7*, e34334. https://doi.org/10.7554/eLife.34334.
44. Porter, D.J., Merrill, B.M., and Short, S.A. (1995). Identification of the active site nucleophile in nucleoside 2-deoxyribosyltransferase as glutamic acid 98. J. Biol. Chem. *270*, 15551–15556. https://doi.org/10.1074/jbc.270.26.15551.
45. Armstrong, S.R., Cook, W.J., Short, S.A., and Ealick, S.E. (1996). Crystal structures of nucleoside 2-deoxyribosyltransferase in native and ligand-bound forms reveal architecture of the active site. Structure *4*, 97–107. https://doi.org/10.1016/s0969-2126(96)00013-5.
46. Anand, R., Kaminski, P.A., and Ealick, S.E. (2004). Structures of purine 2′-deoxyribosyltransferase, substrate complexes, and the ribosylated enzyme intermediate at 2.0 A resolution. Biochemistry *43*, 2384–2393. https://doi.org/10.1021/bi035723k.
47. Dupouy, C., Zhang, C., Padilla, A., Pochet, S., and Kaminski, P.A. (2010). Probing the active site of the deoxynucleotide N-hydrolase Rcl encoded by the rat gene c6orf108. J. Biol. Chem. *285*, 41806–41814. https://doi.org/10.1074/jbc.M110.181594.
48. Tang, P., Harding, C.J., Dickson, A.L., da Silva, R.G., Harrison, D.J., and Czekster, C.M. (2024). Snapshots of the reaction coordinate of a thermophilic 2′-deoxyribonucleoside/ribonucleoside transferase. ACS Catal. *14*, 3090–3102. https://doi.org/10.1021/acscatal.3c06260.
49. Macnutt, W.S. (1952). The enzymically catalysed transfer of the deoxyribosyl group from one purine or pyrimidine to another. Biochem. J. *50*, 384–397. https://doi.org/10.1042/bj0500384.
50. Sikowitz, M.D., Cooper, L.E., Begley, T.P., Kaminski, P.A., and Ealick, S.E. (2013). Reversal of the substrate specificity of CMP N-glycosidase to dCMP. Biochemistry *52*, 4037–4047. https://doi.org/10.1021/bi400316p.
51. Liu, Q., Kriksunov, I.A., Graeff, R., Munshi, C., Lee, H.C., and Hao, Q. (2006). Structural basis for the mechanistic understanding of human CD38-controlled multiple catalysis. J. Biol. Chem. *281*, 32861–32869. https://doi.org/10.1074/jbc.M606365200.
52. Manik, M.K., Shi, Y., Li, S., Zaydman, M.A., Damaraju, N., Eastman, S., Smith, T.G., Gu, W., Masic, V., Mosaiab, T., et al. (2022). Cyclic ADP ribose isomers: production, chemical structures, and immune signaling. Science *377*, eadc8969. https://doi.org/10.1126/science.adc8969.
53. Stokar-Avihail, A., Fedorenko, T., Hör, J., Garb, J., Leavitt, A., Millman, A., Shulman, G., Wojtania, N., Melamed, S., Amitai, G., and Sorek, R. (2023). Discovery of phage determinants that confer sensitivity to bacterial immune systems. Cell *186*, 1863–1876.e16. https://doi.org/10.1016/j.cell.2023.02.029.
54. Forsberg, B.O., Shah, P.N.M., and Burt, A. (2023). A robust normalized local filter to estimate compositional heterogeneity directly from cryo-EM maps. Nat. Commun. *14*, 5802. https://doi.org/10.1038/s41467-023-41478-1.
55. Mayo-Muñoz, D., Pinilla-Redondo, R., Camara-Wilpert, S., Birkholz, N., and Fineran, P.C. (2024). Inhibitors of bacterial immune systems: discovery, mechanisms and applications. Nat. Rev. Genet. *25*, 237–254. https://doi.org/10.1038/s41576-023-00676-9.
56. Blower, T.R., Evans, T.J., Przybilski, R., Fineran, P.C., and Salmond, G.P.C. (2012). Viral evasion of a bacterial suicide system by RNA-based molecular mimicry enables infectious altruism. PLoS Genet. *8*, e1003023. https://doi.org/10.1371/journal.pgen.1003023.
57. Srikant, S., Guegler, C.K., and Laub, M.T. (2022). The evolution of a counter-defense mechanism in a virus constrains its host range. eLife *11*, e79549. https://doi.org/10.7554/eLife.79549.

58. Leavitt, A., Yirmiya, E., Amitai, G., Lu, A., Garb, J., Herbst, E., Morehouse, B.R., Hobbs, S.J., Antine, S.P., Sun, Z.J., et al. (2022). Viruses inhibit TIR gcADPR signalling to overcome bacterial defence. Nature *611*, 326–331. https://doi.org/10.1038/s41586-022-05375-9.

59. Bruria, S., and David, B. (2023). A diverse repertoire of anti-defense systems is encoded in the leading region of plasmids. Preprint at bioRxiv. https://doi.org/10.1101/2023.02.15.528439.

60. Pinilla-Redondo, R., Shehreen, S., Marino, N.D., Fagerlund, R.D., Brown, C.M., Sørensen, S.J., Fineran, P.C., and Bondy-Denomy, J. (2020). Discovery of multiple anti-CRISPRs highlights anti-defense gene clustering in mobile genetic elements. Nat. Commun. *11*, 5652. https://doi.org/10.1038/s41467-020-19415-3.

61. Frelin, O., Huang, L., Hasnain, G., Jeffryes, J.G., Ziemak, M.J., Rocca, J.R., Wang, B., Rice, J., Roje, S., Yurgel, S.N., et al. (2015). A directed-overflow and damage-control N-glycosidase in riboflavin biosynthesis. Biochem. J. *466*, 137–145. https://doi.org/10.1042/BJ20141237.

62. de Souza, R.F., and Aravind, L. (2012). Identification of novel components of NAD-utilizing metabolic pathways and prediction of their biochemical functions. Mol. Biosyst. *8*, 1661–1677. https://doi.org/10.1039/c2mb05487f.

63. Jumper, J., Evans, R., Pritzel, A., Green, T., Figurnov, M., Ronneberger, O., Tunyasuvunakool, K., Bates, R., Žídek, A., Potapenko, A., et al. (2021). Highly accurate protein structure prediction with AlphaFold. Nature *596*, 583–589. https://doi.org/10.1038/s41586-021-03819-2.

64. Groslambert, J., Prokhorova, E., and Ahel, I. (2021). ADP-ribosylation of DNA and RNA. DNA Repair (Amst) *105*, 103144. https://doi.org/10.1016/j.dnarep.2021.103144.

65. Hogrel, G., Guild, A., Graham, S., Rickman, H., Grüschow, S., Bertrand, Q., Spagnolo, L., and White, M.F. (2022). Cyclic nucleotide-induced helical structure activates a TIR immune effector. Nature *608*, 808–812. https://doi.org/10.1038/s41586-022-05070-9.

66. Morehouse, B.R., Yip, M.C.J., Keszei, A.F.A., McNamara-Bordewick, N.K., Shao, S., and Kranzusch, P.J. (2022). Cryo-EM structure of an active bacterial TIR–STING filament complex. Nature *608*, 803–807. https://doi.org/10.1038/s41586-022-04999-1.

67. Wang, M., Ji, Q., Liu, P., and Liu, Y. (2023). NAD(+) depletion and defense in bacteria. Trends Microbiol. *31*, 435–438. https://doi.org/10.1016/j.tim.2022.06.002.

68. Cao, X., Xiao, Y., Huiting, E., Cao, X., Li, D., Ren, J., Fedorova, I., Wang, H., Guan, L., Wang, Y., et al. (2024). Phage anti-CBASS protein simultaneously sequesters cyclic trinucleotides and dinucleotides. Mol. Cell *84*, 375–385.e7. https://doi.org/10.1016/j.molcel.2023.11.026.

69. Jenson, J.M., Li, T., Du, F., Ea, C.K., and Chen, Z.J. (2023). Ubiquitin-like conjugation by bacterial cGAS enhances anti-phage defence. Nature *616*, 326–331. https://doi.org/10.1038/s41586-023-05862-7.

70. Yirmiya, E., Leavitt, A., Lu, A., Ragucci, A.E., Avraham, C., Osterman, I., Garb, J., Antine, S.P., Mooney, S.E., Hobbs, S.J., et al. (2024). Phages overcome bacterial immunity via diverse anti-defence proteins. Nature *625*, 352–359. https://doi.org/10.1038/s41586-023-06869-w.

71. Wein, T., and Sorek, R. (2022). Bacterial origins of human cell-autonomous innate immune mechanisms. Nat. Rev. Immunol. *22*, 629–638. https://doi.org/10.1038/s41577-022-00705-4.

72. Carabias, A., Fuglsang, A., Temperini, P., Pape, T., Sofos, N., Stella, S., Erlendsson, S., and Montoya, G. (2021). Structure of the mini-RNA-guided endonuclease CRISPR-Cas12j3. Nat. Commun. *12*, 4476. https://doi.org/10.1038/s41467-021-24707-3.

73. Meier-Kolthoff, J.P., and Göker, M. (2017). VICTOR: genome-based phylogeny and classification of prokaryotic viruses. Bioinformatics *33*, 3396–3404. https://doi.org/10.1093/bioinformatics/btx440.

74. Bouras, G., Nepal, R., Houtak, G., Psaltis, A.J., Wormald, P.-J., and Vreugde, S. (2023). Pharokka: a fast scalable bacteriophage annotation tool. Bioinformatics *39*, btac776. https://doi.org/10.1093/bioinformatics/btac776.

75. Terzian, P., Olo Ndela, E., Galiez, C., Lossouarn, J., Pérez Bucio, R.E., Mom, R., Toussaint, A., Petit, M.-A., and Enault, F. (2021). PHROG: families of prokaryotic virus proteins clustered using remote homology. NAR Genom. Bioinform. *3*, lqab067. https://doi.org/10.1093/nargab/lqab067.

76. van Kempen, M., Kim, S.S., Tumescheit, C., Mirdita, M., Lee, J., Gilchrist, C.L.M., Söding, J., and Steinegger, M. (2024). Fast and accurate protein structure search with Foldseek. Nat. Biotechnol. *42*, 243–246. https://doi.org/10.1038/s41587-023-01773-0.

77. Varadi, M., Anyango, S., Deshpande, M., Nair, S., Natassia, C., Yordanova, G., Yuan, D., Stroe, O., Wood, G., Laydon, A., et al. (2022). AlphaFold Protein Structure Database: massively expanding the structural coverage of protein-sequence space with high-accuracy models. Nucleic Acids Res. *50*, D439–D444. https://doi.org/10.1093/nar/gkab1061.

78. Katoh, K., and Standley, D.M. (2013). MAFFT multiple sequence alignment software version 7: improvements in performance and usability. Mol. Biol. Evol. *30*, 772–780. https://doi.org/10.1093/molbev/mst010.

79. Price, M.N., Dehal, P.S., and Arkin, A.P. (2010). FastTree 2--approximately maximum-likelihood trees for large alignments. PLoS One *5*, e9490. https://doi.org/10.1371/journal.pone.0009490.

80. Punjani, A., Rubinstein, J.L., Fleet, D.J., and Brubaker, M.A. (2017). cryoSPARC: algorithms for rapid unsupervised cryo-EM structure determination. Nat. Methods *14*, 290–296. https://doi.org/10.1038/nmeth.4169.

81. Goddard, T.D., Huang, C.C., Meng, E.C., Pettersen, E.F., Couch, G.S., Morris, J.H., and Ferrin, T.E. (2018). UCSF ChimeraX: meeting modern challenges in visualization and analysis. Protein Sci. *27*, 14–25. https://doi.org/10.1002/pro.3235.

82. Adams, P.D., Afonine, P.V., Bunkóczi, G., Chen, V.B., Davis, I.W., Echols, N., Headd, J.J., Hung, L.W., Kapral, G.J., Grosse-Kunstleve, R.W., et al. (2010). Phenix: a comprehensive Python-based system for macromolecular structure solution. Acta Crystallogr. D Biol. Crystallogr. *66*, 213–221. https://doi.org/10.1107/S0907444909052925.

83. Emsley, P., Lohkamp, B., Scott, W.G., and Cowtan, K. (2010). Features and development of coot. Acta Crystallogr. D Biol. Crystallogr. *66*, 486–501. https://doi.org/10.1107/S0907444910007493.

84. Smart, O.S., A., S., Holstein, J., Womack, T.O., Flensburg, C., Keller, P., Paciorek, W., Vonrhein, C., and Bricogne, G. (2021). Grade2 version 1.5.0 (Global Phasing Ltd).

85. Ashkenazy, H., Abadi, S., Martz, E., Chay, O., Mayrose, I., Pupko, T., and Ben-Tal, N. (2016). ConSurf 2016: an improved methodology to estimate and visualize evolutionary conservation in macromolecules. Nucleic Acids Res. *44*, W344–W350. https://doi.org/10.1093/nar/gkw408.

86. Robert, X., and Gouet, P. (2014). Deciphering key features in protein structures with the new ENDscript server. Nucleic Acids Res. *42*, W320–W324. https://doi.org/10.1093/nar/gku316.

87. Deatherage, D.E., and Barrick, J.E. (2014). Identification of mutations in laboratory-evolved microbes from next-generation sequencing data using breseq. Methods Mol. Biol. *1151*, 165–188. https://doi.org/10.1007/978-1-4939-0554-6_12.

88. Tal, N., Millman, A., Stokar-Avihail, A., Fedorenko, T., Leavitt, A., Melamed, S., Yirmiya, E., Avraham, C., Brandis, A., Mehlman, T., et al. (2022). Bacteria deplete deoxynucleotides to defend against bacteriophage infection. Nat. Microbiol. *7*, 1200–1209. https://doi.org/10.1038/s41564-022-01158-0.

89. Hsiao, J.J., Potter, O.G., Chu, T.W., and Yin, H. (2018). Improved LC/MS methods for the analysis of metal-sensitive analytes using medronic acid as a mobile phase additive. Anal. Chem. *90*, 9457–9464. https://doi.org/10.1021/acs.analchem.8b02100.

90. Bepler, T., Morin, A., Rapp, M., Brasch, J., Shapiro, L., Noble, A.J., and Berger, B. (2019). Positive-unlabeled convolutional neural networks for

particle picking in cryo-electron micrographs. Nat. Methods *16*, 1153–1160. https://doi.org/10.1038/s41592-019-0575-8.

91. Tyanova, S., Temu, T., and Cox, J. (2016). The MaxQuant computational platform for mass spectrometry-based shotgun proteomics. Nat. Protoc. *11*, 2301–2319. https://doi.org/10.1038/nprot.2016.136.
92. Jakočiūnė, D., and Moodley, A. (2018). A rapid bacteriophage DNA extraction method. Methods Protoc. *1*, 27. https://doi.org/10.3390/mps1030027.
93. Dong, R., Peng, Z., Zhang, Y., and Yang, J. (2018). mTM-align: an algorithm for fast and accurate multiple protein structure alignment. Bioinformatics *34*, 1719–1725. https://doi.org/10.1093/bioinformatics/btx828.

STAR★METHODS

KEY RESOURCES TABLE

REAGENT or RESOURCE	SOURCE	IDENTIFIER
Antibodies		
Rabbit Poly/Mono-ADP Ribose	Cell Signaling Technology	Cat# 83732; RRID:AB_2749858
Goat Anti-Rabbit IgG - H&L Polyclonal antibody, Hrp Conjugated	Abcam	Cat# ab6721; RRID:AB_955447
Bacterial and virus strains		
E.coli BL21(DE3) Competent Cells	Thermo Scientific	Cat# EC0114
E.coli MG1655	Søren J. Sørensen Lab, Copenhagen University, DK	NCBI: NC_000913
E.coli MG1655(DE3)	This Paper	N/A
E.coli Stellar Competent Cells	Takara Bio	Cat# 636766
NEB 5-alpha Competent *E. coli* (High Efficiency)	New England Biolabs	Cat# C2987H
Lambda Vir phage	Bondy Denomy Lab, UCSF, USA	N/A
Escherichia phage Tonn	Olsen et al.[32]	NCBI: NC_049815
Escherichia phage Ffm	Kind gift from Jakob Bobonis, EMBL.	DSMZ: DSM 18264
T4 phage	Kind gift from Claudia Igler, ETH	N/A
T6 phage	Kind gift from Claudia Igler, ETH	N/A
Escherichia phage Teqhad	Olsen et al.[32]	GenBank: MN895434.1
T2 phage	Bobonis et al.[20]	N/A
T5 phage	Kind gift from Claudia Igler, ETH.	N/A
Escherichia phage Anhysbus	Olsen et al.[32]	GenBank: MN850648.1
Escherichia phage Ukendt	Olsen et al.[32]	NCBI: NC_052661.1
Escherichia phage Muut	Olsen et al.[32]	NCBI: NC_052657.1
Biological samples		
λDE3 Lysogenization Kit	Novagen	Cat# 69734-M
Chemicals, peptides, and recombinant proteins		
β-Nicotinamide adenine dinucleotide (NAD), reduced disodium salt hydrate	Sigma Aldrich	Cat# N8129-100MG
Adenosine 5′-diphosphoribose (ADPr) sodium salt	Sigma Aldrich	Cat# A0752
Nicotinamide (Nam)	Sigma Aldrich	Cat# 72340
GelRed Nucleic Acid Stain (10000X DMSO)	Millipore	Cat# SCT122
InstantBlue protein Gel Staining	Sigma Aldrich	Cat# ISB1L
ss20 DNA Ladder (100uL)	Fisher Scientific; Simplex Sciences	Cat# NC2177719
Hydroxylamine	Sigma Aldrich	Cat #467804
Critical commercial assays		
CloneAmp HiFi PCR Premix	Takara Bio	Cat# 639298
In-Fusion Snap Assembly Master Mix	Takara Bio	Cat# 638948
Deposited data		
Model of Retron-Eco1-WT+NAD^+ (Full map, 2 segments)	This paper	PDB: 8QBM
Model of Retron-Eco1-WT+NAD^+ (Local map, 1 segment)	This paper	PDB: 8QBK
Model of Retron-Eco1-E106A	This paper	PDB: 8QBL
Retron-Eco1-WT	This paper	EMDB:18317

(*Continued on next page*)

Continued

REAGENT or RESOURCE	SOURCE	IDENTIFIER
Map of Retron-Eco1-WT+NAD$^+$ (Full map, 2 segments)	This paper	EMDB:18315
Map of Retron-Eco1-WT+NAD$^+$ (Local map, 1 segment)	This paper	EMDB:18313
Map of Retron-Eco1-WT+NAD$^+$ (Consensus refinement)	This paper	EMDB:19793
Map of Retron-Eco1-E106A	This paper	EMDB:18314
Map of Retron-Eco1 -1 turn mutant (Consensus refinement)	This paper	EMDB:19792
Raw and analyzed ADP-ribosylation MS data	This paper	ProteomeXchange: PXD044835
Uncropped and uncompressed imaging data and.nex files for trees and alignments of U69 and U56	This paper	Mendeley Data: 10.17632/sbwfyh2btr.1
Oligonucleotides		
Primers used for cloning and site-directedmutagenesis and oligonucleotides used in ADP-ribosylation assays are listed in	This paper	Table S4
Recombinant DNA		
pLG001 (pACYC184 empty vector; low copy number plasmid; Cam^R)	Gao et al.[22]	Addgene plasmid 157879
pLG007 (pACYC184 vector carrying Retron-Eco1 expressed under its endogenous promoter; Cam^R)	Gao et al.[22]	Addgene plasmid 157885
pLG007-Tagged (pACYC184 vector carrying Retron-Eco1-Tagged [RT-TwinStrep; Effector-FLAG]; Cam^R)	This paper	N/A
pLG007-Tagged-RT-Δ1-14 (pACYC184 vector carrying Retron-Eco1-Tagged mutant lacking the helix α-1 of the RT; Cam^R)	This paper	N/A
pLG007-Tagged-RT-D197N/D198N (pACYC184 vector carrying Retron-Eco1-Tagged RT-mutant D197N/D198N; Cam^R)	This paper	N/A
pLG007-Tagged-RT-D119N (pACYC184 vector carrying Retron-Eco1-Tagged RT-mutant D119N; Cam^R)	This paper	N/A
pLG007-Tagged-RT-R70A/A74R (pACYC184 vector carrying Retron-Eco1-Tagged RT-mutant R70A/A74R; Cam^R)	This paper	N/A
pLG007-Tagged-msr+5poliA (pACYC184 vector carrying Retron-Eco1-Tagged msr-mutant with 5-poliA after the nucleotide msr66; Cam^R)	This paper	N/A
pLG007-Tagged-msr+10poliA (pACYC184 vector carrying Retron-Eco1-Tagged msr-mutant with 10-poliA after the nucleotide msr66; Cam^R)	This paper	N/A
pLG007-Tagged-msr+15poliA (pACYC184 vector carrying Retron-Eco1-Tagged msr-mutant with 15-poliA after the nucleotide msr66; Cam^R)	This paper	N/A

(*Continued on next page*)

Continued

REAGENT or RESOURCE	SOURCE	IDENTIFIER
pLG007-Tagged-Effector-R292A/R293A/K294A (pACYC184 vector carrying Retron-Eco1-Tagged Effector-mutant R292A/R293A/K294A; Cam^R)	This paper	N/A
pLG007-Tagged-Effector-E106A (pACYC184 vector carrying Retron-Eco1-Tagged Effector-mutant E106A; Cam^R)	This paper	N/A
pLG007-Tagged-Effector-E106Q (pACYC184 vector carrying Retron-Eco1-Tagged Effector-mutant E106Q; Cam^R)	This paper	N/A
pLG007-Tagged-Effector-E84A (pACYC184 vector carrying Retron-Eco1-Tagged Effector-mutant E84A; Cam^R)	This paper	N/A
pLG007-Tagged-Effector-F33Y (pACYC184 vector carrying Retron-Eco1-Tagged Effector-mutant F33Y; Cam^R)	This paper	N/A
pLG007-Tagged-Effector-T105R (pACYC184 vector carrying Retron-Eco1-Tagged Effector-mutant T105R; Cam^R)	This paper	N/A
pLG007-Tagged-Effector-N112A (pACYC184 vector carrying Retron-Eco1-Tagged Effector-mutant N112A; Cam^R)	This paper	N/A
pLG007-Tagged-Effector-Y137R (pACYC184 vector carrying Retron-Eco1-Tagged Effector-mutant Y137R; Cam^R)	This paper	N/A
pLG007-Tagged-Effector-F128A/K131A (pACYC184 vector carrying Retron-Eco1-Tagged Effector-mutant F128A/K131A; Cam^R)	This paper	N/A
pET21-cHIS (High copy number plasmid carrying a T7 promoter sequence under the control of Lac operator; Amp^R)	Carabias et al.[72]	N/A
pET21-RT-ncRNA (Vector carrying Retron-Eco1 ncRNA and C-terminal TEV-His-tagged RT used for purification with the effector; Amp^R)	This paper	N/A
pET21-RT-ncRNA-msDNA-Stem(-1 turn) (Vector carrying Retron-Eco1 msDNA Stem-mutant lacking 1-helix turn [ΔmsDNA31-54]; Amp^R)	This paper	N/A
pET21-RT-ncRNA-msDNA-Stem(-2 turn) (Vector carrying Retron-Eco1 msDNA Stem-mutant lacking 2-helix turns [ΔmsDNA21-64]; Amp^R)	This paper	N/A
pACYC-Duet-1 (Low copy number plasmid carrying a T7 promoter sequence under the control of Lac operator; Cam^R)	Sigma Aldrich; Novagen	Cat# 71147
pACYC-Duet-Effector (Vector carrying Retron-Eco1 Effector without a tag used for purification with the ncRNA and RT; Cam^R)	This paper	N/A
pACYC-Duet-Effector-E106A (Vector carrying Retron-Eco1 Effector mutant E106A; Cam^R)	This paper	N/A
pACYC-Duet-Effector-E106Q (Vector carrying Retron-Eco1 Effector mutant E106Q; Cam^R)	This paper	N/A
pACYC-Duet-Effector-F128A/K131A (Vector carrying Retron-Eco1 Effector mutant F128A/K131A; Cam^R)	This paper	N/A
pACYC-Duet-Effector-E114Q (Vector carrying Retron-Eco1 Effector mutant E114Q; Cam^R)	This paper	N/A

(*Continued on next page*)

Continued

REAGENT or RESOURCE	SOURCE	IDENTIFIER
pACYC-Duet-Effector-T105R (Vector carrying Retron-Eco1 Effector mutant T105R; Cam^R)	This paper	N/A
pACYC-Duet-Effector-N112A (Vector carrying Retron-Eco1 Effector mutant N112A; Cam^R)	This paper	N/A
pACYC-Duet-Effector-Y137R (Vector carrying Retron-Eco1 Effector mutant Y137R; Cam^R)	This paper	N/A
pET21-U56-cHIS (Vector carrying U56 with c-Terminal TEV-HIS tag, Amp^R)	This paper	N/A
pHerd30T (high-copy-number plasmid carrying an arabinose promoter sequence [PBAD]; Empty vector control for activator and repressor expression; Gm^R)	Pinilla-Redondo et al.[60] (NovoPro Vector)	Cat# V005565
pHerd-U54 (Vector carrying *Ukendt_54* under PBAD promoter; Gm^R)	This paper	N/A
pHerd-U55 (Vector carrying *Ukendt_55* under PBAD promoter; Gm^R)	This paper	N/A
pHerd-U56 (Vector carrying *Ukendt_56* under PBAD promoter; Gm^R)	This paper	N/A
pHerd-U69 (Expression of protein *Ukendt_69* under PBAD promoter; Gm^R)	This paper	N/A
pHerd-U56-E127A (Vector carrying *Ukendt_56* mutant E127A under PBAD promoter; Gm^R)	This paper	N/A
pHerd-U56-E127Q (Vector carrying *Ukendt_56* mutant E127Q under PBAD promoter; Gm^R)	This paper	N/A
pHerd-U56-E40A (Vector carrying *Ukendt_56* mutant E40A under PBAD promoter; Gm^R)	This paper	N/A
pHerd-U56-E40Q (Vector carrying *Ukendt_56* mutant E40Q under PBAD promoter; Gm^R)	This paper	N/A
Software and algorithms		
OccuPy	Forsberg et al.[54]	https://occupy.readthedocs.io/en/latest/
AlphaFold2 - Colaboratory	Jumper et al.[63]	https://colab.research.google.com/github/sokrypton/ColabFold/blob/main/AlphaFold2.ipynb
VICTOR web service	Meier-Kolthoff and Göker[73]	https://ggdc.dsmz.de/victor.php
Pharokka	Bouras et al.[74]	https://github.com/gbouras13/pharokka
PHROGs database	Terzian et al.[75]	https://phrogs.lmge.uca.fr/
Foldseek	van Kempen et al.[76]	https://search.foldseek.com/search
HMMER 3.3.2	N/A	hmmer.org
Alphafold protein structure database	Varadi et al.[77]	https://alphafold.ebi.ac.uk/
mafft-ginsi	Katoh and Standley[78]	https://mafft.cbrc.jp/alignment/software/
FastTree2	Price et al.[79]	http://www.microbesonline.org/fasttree/
CryoSPARC v4.2.1	Punjani et al.[80]	https://cryosparc.com
Chimera X 1.6.1	Goddard et al.[81]	https://preview.rbvi.ucsf.edu/chimerax/
Phenix 1.19-4092	Adams et al.[82]	https://phenix-online.org/
Coot 0.9.6	Emsley et al.[83]	https://www2.mrc-lmb.cam.ac.uk/personal/pemsley/coot/
Grade2 server	Smart et al.[84]	https://grade.globalphasing.org
Consurf server	Ashkenazy et al.[85]	http://consurf.tau.ac.il

(*Continued on next page*)

Continued		
REAGENT or RESOURCE	SOURCE	IDENTIFIER
ESPript3 server	Robert and Gouet[86]	https://espript.ibcp.fr/ESPript/ESPript/
breseq 0.37.0	Deatherage and Barrick[87]	https://barricklab.org/release/breseq/
Prism 9	Graphpad by Dotmatics	https://www.graphpad.com/
Adobe Illustrator 2023	Adobe	https://www.adobe.com/
Other		
NuPAGE® 4-12% Bis Tris Gel (1.5 mm, 15 Well)	Invitrogen™	Cat# NP0336BOX
iBlot® Transfer Stack, Mini (Nitrocellulose)	Invitrogen™	Cat# IB301032
E-Gel Agarose Gels (1%, SYBR safe DNA stain)	Invitrogen™	Cat# A45203
iBlot™ DNA Transfer Stack	Invitrogen™	Cat# IB801001
SuperSignal™ West Pico PLUS Chemiluminescent Substrate	Thermo Scientific	Cat# 34577
HisTrap FF Crude (5mL)	Merck; Cytiva	Cat# 17528601
HiTrap Q FF (5ml column)	Merck; Cytiva	Cat# 17515601
Superose 6 Increase 3.2/300	Cytiva	Cat# 29091598
CryoEM grids (1.2/1.3, 200 mesh)	Quantifoil	Cat# S143-1
Negative staining grids (Cu100, 300 mesh)	EM Resolutions	Cat# C300Cu100

RESOURCE AVAILABILITY

Lead contact

Further information and requests for resources and reagents should be directed to and will be fulfilled by the lead contact, Guillermo Montoya (guillermo.montoya@cpr.ku.dk).

Materials availability

All reagents generated in this study are available upon request to the lead contact with a completed Materials Transfer Agreement.

Data and code availability

- The structure's atomic coordinates and cryoEM maps have been deposited in the PDB (https://www.rcsb.org) and EMDB (https://www.ebi.ac.uk/emdb/) databases. Raw and analyzed ADP-ribosylation MS data have been deposited in the ProteomeXchange database (https://www.proteomexchange.org/) MS data Uncropped imaging data have been deposited at Mendeley Data (https://data.mendeley.com/). Accession numbers and DOIs are listed in the key resources table.
- This paper does not report original code.
- Any additional information required to reanalyze the data reported in this paper is available from the lead contact upon request.

EXPERIMENTAL MODEL AND STUDY PARTICIPANT DETAILS

Microbe strains

The key resources table contains a list of the phages and bacterial strains used in this work. *E. coli* Stellar (Takara Bio, 636766) and NEB 5-alpha (New England Biolabs C2987H) strains were used for plasmid production. Phage infection assays were performed with *E. coli* MG1655 strain. *E. coli* BL21(DE3) strain (Thermo Scientific, EC0114) and a custom-made MG1655(DE3) strain (prepared with the λDE3 Lysogenization Kit, Novagen, 69734-M) were used for protein expression. Cells were grown in LB or Terrific Broth supplemented with appropriate antibiotics at standard temperatures (37°C). See the methods details for further information about the propagation and maintenance of the bacteria and phages.

METHOD DETAILS

DNA and molecular biology

Plasmids and constructs

For the construction of expression vectors, we performed USER cloning (NEB) or Gibson Assembly (NEB) following the manufacturer's instructions using the primers listed in Table S4. pLG001 (empty vector) and pLG007 (Ec86 retron) were a gift from Feng Zhang (Addgene plasmids # 157879 [http://n2t.net/addgene:157879; RRID:Addgene_157879] and # 157885 [http://n2t.net/addgene:157885; RRID:Addgene_157885]). A twin-strep Tag and a FLAG tag were included downstream of the Eco1-RT and downstream

of the Eco1-effector respectively (pLG007-tagged) (Twist Bioscience). pLG007-tagged plasmid was used for functional assays. The Retron-Eco1 ncRNA (comprising the *a1*, *a2*, *msr* and *msd* regions) and the reverse transcriptase (RT) C-terminally tagged with a recognition site for the TEV protease and a hexa-his tag was cloned in pET21a[72] (pET21a-RT-ncRNA) and used for overexpression and purification. A ribosome binding site (RBS) was included upstream of the RT gene after the *a2* region to improve the expression of the protein. The effector complex was cloned in pACYC-Duet (pACYC-Duet-Effector), without including tags. *U56* was cloned into a pET21a vector upstream of the sequence coding for a TEV-HIS tag. The mutants in the manuscript were generated by site-directed mutagenesis using the infusion cloning kit (Takara) and the primers described in the Table S4. Mutants T105R, N112A, Y137R, E84A and F33Y were custom generated (Genewiz). The mutants were generated in the pLG007-tagged plasmid backbone, except for the shortened msDNA mutants (-1 turn and -2 turn) that yielded no positive clones when they were cloned in pLG007-tagged plasmid, suggesting their toxicity. We only obtained positive clones using the inducible-expression plasmid pET21a-RT-ncRNA. For functional testing of inhibitor and activator candidates, *U54*, *U55*, *U56* and *U69* were cloned into pHerd30T downstream of the P_{BAD} promoter.

Extraction of msDNA

Liquid cultures of the bacteria (4 mL) containing the pLG007-tagged plasmids (WT and mutants) were grown to a OD_{600nm} of 0.3. The msDNA was extracted from the bacteria using a miniprep kit (macherey-nagel) or by phenol: chloroform extraction followed by treatment with 100 μg/ml of RNAse A at 20°C for 10 min. For the analysis of the nucleic acids bound to the recombinant complexes (Figure S1D), ∼10 μgs of the samples were treated at 95°C for 5 min (labelled as "Heatshock") and/or incubated with RNAseA (labelled as "RNAse A"). the size of the nucleic acids was estimated by comparison with ss20 DNA Ladder (simplex sciences) by denaturing electrophoresis using TBE-Urea gels (10%, Novex)

Phage infection assays

Phage propagation

The phages utilized in this research are itemized in the key resources table. In brief, 3 mL of host culture at an optical density (OD) of 0.6 were inoculated with 2 μL from the phage stock. The culture was cultivated for 3 hours and subsequently introduced into 20 mL of host culture with an OD of 1. This mixture was then allowed to grow for 6 hours or until it became clear. To separate the virions from cell debris, a centrifugation step was performed (3,220 × g for 20 minutes at 4°C). The resulting supernatant was filtered under sterile conditions into a universal container for storage. Ultimately, the phage titre was ascertained by pipetting 20 μL droplets of serial dilutions onto a LBA overlay (0.35% w/v) that was seeded with 150 μL of host overnight culture. After an overnight incubation, plaques were enumerated, with the phage titre presented as plaque-forming units per milliliter (PFU/mL). In all assays involving the addition of phages, LB media was supplemented with 10 mM $MgSO_4$.

Plaque assays

For phage plaque assays, triplicate cultures of *E. coli* MG1655 carrying either a plasmid expressing Eco1 (+Eco1) or an empty vector control (-Eco1) were grown in 5 mL LB supplemented with the appropriate antibiotics and inducers. Additional proteins were expressed from an additional plasmid to test potential inhibitor candidates when appropriate (U54, U55, U56, or empty vector, respectively). A soft LB-agar overlay (0.5% w/v), totalling 4mL, was prepared and combined with 150 μL of overnight cultures. This mixture was supplemented with 10 mM $MgSO_4$ and poured onto an LBA plate that was also supplemented with 10 mM $MgSO_4$, along with the corresponding antibiotics and inducers. To determine phage titers, droplets of serially diluted phage stock in phage buffer were pipetted onto the agar overlay. The plates were then incubated overnight, and after the incubation period, the plaques were counted to calculate the phage titer in PFU/mL. The fold reduction of infection was determined by dividing the efficiency of plating (in PFU/mL) of the empty vector by the efficiency of plating on *E. coli* expressing Retron-Eco1.

Phage-infection in liquid medium

Phage infection in liquid media was performed as described previously.[17] In brief, *E. coli* MG1655 cultures were grown overnight, carrying either a plasmid expressing Eco1 or an empty vector as a control. These cultures were then diluted 1:100 in LB medium (10mM $MgSO_4$), and incubated at 37 °C with agitation at 200 rpm until they reached the early log phase (OD_{600nm} = 0.3). Subsequently, 180 μl of the diluted culture was placed into the wells of a 96-well plate. To these wells, 20 μL of phage lysate was added, resulting in a final MOI of 0.02, 0.2, 5, or 20 μL of media for the uninfected control wells. During shaking, the OD_{600nm} was recorded by measuring it every 2 minutes at 37 °C for 350 min.

Phage and protein trees and comparisons

Phage tree comparison

To compare the genomes of all the phages against which we tested the activity of the retron and to construct a phylogenetic tree based on whole-genome data, we utilized the VICTOR web service.[73] Then, the genomes of the phages were re-annotated using the software Pharokka[74] and the PHROGs database.[75]

Structure-based tree of effector homologs

To identify proteins structurally similar to the retron effector, a search was executed using Foldseek[76] against the Protein Data Bank (PDB) and AlphaFold/UniprotKB5 databases[77] with the TM-align algorithm using only the NDT domain of the effector protein as a query. Hits with a TM-align score exceeding 0.5 were shortlisted for further analysis. To minimize redundancy and circumvent over-representation of certain domains, the sequences identified by Foldseek were clustered based on 90% sequence identity over the aligned region. A representative sequence from each cluster was selected, resulting in approximately 620 structural

homologs. After sequence selection, pairwise structural evaluations were conducted employing TM-align. A distance matrix was then built using the RMSD value normalized by the inverse of the number of aligned residues. A dendrogram/tree was synthesized from the distance matrix employing the neighbor-joining algorithm. Additional metadata, collated from database information and manual analysis of select hits, was subsequently appended to the tree.

U69 phylogenetic tree

To identify homologs of the U69 protein in other organisms, we conducted homology searches in the NCBI nr database (https://ftp.ncbi.nlm.nih.gov/blast/db/FASTA/nr.gz). Given the small size of the protein (48aa) and the absence of conserved known domains, we chose to use jackhmmer from the suite HMMER 3.3.2 (hmmer.org) for this search. We executed two iterations of jackhmmer using default parameters. Following this, we removed sequence redundancy using CD-HIT 10 at 100% sequence identity, conducted an alignment using mafft-ginsi[78] and performed a phylogenetic reconstruction with FastTree2.[79] The nex files for the phylogenetic tree and the alignment are deposited in Mendeley Data.

NADAR phylogenetic analysis

To predict the activity and classification of U56, we conducted phylogenetic analyses using data from previously published studies on various NADAR proteins.[18,62] The sequences were aligned using mafft-ginsi[78] with default parameters. Subsequently, positions containing more than 90% gaps were excluded. A phylogenetic reconstruction was then performed using FastTree2[79] with default settings. Lastly, the phylogenetic tree was annotated using metadata from the original publications. U56 was further compared with *Pn*NADAR structurally, by superposing the *Pn*NADAR structure (PDB: 8BAU) with a U56 AlphaFold2[63] model (RMSD: 3.04 7Å across 162 pairs). The nex files for the phylogenetic tree and the alignment are deposited in Mendeley Data.

Protein expression and purification

Retron-Eco1-WT complexes were expressed in *E. coli* BL21(DE3). Retron-Eco1-Mutant complexes were expressed in an MG1655(DE3) custom-made strain (created with DE3-lysogenization kit, Novagen), to avoid contamination with endogenous Retron-Eco1. BL21(DE3) and MG1655(DE3) strains were transformed with pET21a -RT-ncRNA and pACYC-Duet-Effector. Cultures were grown at 37 °C in a liquid Terrific Broth (TB) medium supplemented with 0.5% glucose, 34 mg/l chloramphenicol and 100 mg/l ampicillin. Cells grew to an optical density at 600 nm of ~0.8 and protein expression was induced by adding 200 nM of IPTG for 3 h at 37 °C. Cells were harvested by centrifugation, flash frozen, and stored at −80°C. The cell pellet was resuspended in lysis buffer (20 mM HEPES pH7.5, 500 mM NaCl, 5 mM $MgCl_2$, 1 tablet of Complete Inhibitor cocktail EDTA Free (Roche) per 50 ml and 1 mg/ml lysozyme). Lysis was completed by one freeze-thaw cycle and sonication. Cell extract was high-speed centrifuged (10,000 × g, 45 min) to separate the soluble fraction from the insoluble fraction and the cell debris. The cell lysate was loaded into a 5 ml HisTrap FF Crude column (Cytiva) equilibrated in buffer IMAC-A (20 mM HEPES pH7.5, 500 mM NaCl, 20 mM Imidazole), and the bound proteins were eluted by a gradient increase of the imidazole concentration with buffer IMAC-B (20 mM HEPES pH7.5, 500 mM NaCl, 500 mM Imidazole). Retron-Eco1 proteins eluted at ~ 150 mM Imidazole. Fractions containing Retron-Eco1 complexes were pooled, diluted to a final NaCl concentration of 150 mM and loaded into a Hitrap-Q column (Cytiva). Retron-Eco1 complexes were eluted by a 150 mM to 2 M NaCl gradient in 20 mM HEPES pH 7.5, 1 mM TCEP buffer. Fractions containing Retron-Eco1 complex, with RT and Effector proteins, and ncRNA-msDNA, were pooled and dialyzed ON at 4°C against the cleavage buffer (20 mM Hepes pH 7.5, 200 mM KCl, 1 mM TCEP). U56-TEV-HIS was expressed and purified by IMAC as Retron-Eco1. The C-terminal His-tag was cleaved by incubation with His-tagged rTEV protease (custom purified) ON at 4°C in TEV buffer (20 mM HEPES pH 7.5, 150 mM NaCl, 1 mM EDTA, 0.5 mM TCEP) for 16 h at 4 °C. U56 was separated from the HIS-tag and the rTEV protease by reverse IMAC, followed by dialysis against the "ITC buffer" (20 mM KPi pH 7.5, 300 mM KCl, 1 mM TCEP). U56 pure protein was flash-frozen and stored at -80°C until the day of the experiment.

In vitro NAD^+ cleavage assays

Sample preparation

In vitro NAD^+ cleavage reactions were performed by incubating 2 μM of Retron-Eco1 complexes with different concentrations of NAD^+ (10μM, 100μM or 1mM) in cleavage buffer (20 mM HEPES pH7.5, 200 mM KCl, 1mM TCEP) at 20°C. The reaction was stopped at different time points. For the kinetic analysis (Michaelis-Menten), 2 μM of Retron-Eco1 was incubated with different NAD^+ concentrations (10, 50, 100, 200, 300, 400, 600, 800, 1000, 2000 μM) in cleavage buffer for 15 min, and the metabolites were extracted as described before. For the activity assay with a pre-ADP-ribosylated complex, Retron-Eco1 was first incubated with 1mM NAD^+ for 1h at 20°C. The ADP-ribosylated complex was purified from the free metabolites by SEC (Superose 6 increase 3.2/300) column equilibrated in "cleavage buffer". The pre-ADP-ribosylated complex (2 μM) was incubated with 10 μM of NAD^+ and the reaction was stopped, and samples were collected at different time points.

LC-MS analysis

The samples for metabolite LC-MS analysis were deproteinized by mixing with ice cold (−20 °C) methanol (1:3, v/v), vortexing for 1 min and keeping them at 20 °C for 60 min. After that, the samples were centrifugated (13000 rcf, 15 min, 4 °C) and the supernatant collected, vacuum dried (SpeedVac) and stored at −20 °C for further processing. The samples (containing ~ 80 pmol NAD^+) were injected into a UPLC system (UltiMate 3000, Dionex) on a Hypercarb column (2.1 mm x 100 mm, 3.0 μm particle size, ThermoFisher Scientific, P/N 35003-102146) and analysed with a microOTOF-Q II mass spectrometer (Bruker Daltonics GmhH) equipped with an electrospray ionization (ESI) source (capillary voltage 4500 V, end plate offset -500 V, nebulizer gas (nitrogen)

pressure 2.0 bar, flow 9 l/min and drying gas temperature 200 °C). The LC method uses a gradient of A (10 mM ammonium acetate, 5 μM medronic acid in water) and B (10 mM ammonium acetate, 5 μM medronic acid, 10% acetonitrile) with a flow rate of 0.15 ml/min as follows: 0-3 min 10% B, 3-4 min 20% B, 4-10 min 40% B, 10-11.5 min 40% B, 11.5-16 min 50% B, 16-22 min 10% B. The column temperature was 50 °C. Mass data were acquired in positive-ion mode with a scan range m/z 300-1500 and a mass resolving power of 10000. Data acquisition was done under the control of the module Hystar 3.2-SR 2 from Bruker Compass 1.3 software that integrates both the LC chromatographic separation and MS methods. The following compounds were purchased from Merck and used as standards for the quantification of the respective compounds by LC-MS analysis: adenosine 5′-diphosphoribose sodium salt (ADPR, P/N A0752), β-Nicotinamide adenine dinucleotide hydrate (NAD^+, P/N 10127965001) and nicotinamide (NAM, P/N 72340). Data analysis was done with DataAnalysis, QuantAnalysis Version 6.0 (Build 434.31.0, Bruker Daltonics GmbH). The concentration of each compound was calculated by measuring the area behind the peaks (UV), using NAD^+, ADPr and Nam standards of known concentrations for calibration. The ''Species ratio'' was calculated by dividing the concentration of each species by the sum of NAD^+ and Nam, except for the E106A mutant in which the NAD^+ was calculated by dividing the concentration of NAD^+ in each point by the initial NAD^+ concentration. A single exponential decay model was fitted to the time-dependent degradation data using Prism, and the fit is shown in the plots, except for Figure S7K in which the dots were connected with a straight line. The apparent speed values (k_{app}) of NAD^+ consumption and ADPr and Nam production for the different retron-Eco1 samples are displayed in Table S1. K_m and V_{max} were calculated by fitting the Michaelis-Menten equation to the experimental data shown in Figure 1F in Prism 9.

Bacterial metabolites detection by LC-MS

Cell lysate preparation

Cell lysates were prepared as previously described.[88] Briefly, we grew overnight cultures of *E. coli* MG1655 either carrying a plasmid expressing Eco1, in the presence or absence of the inhibitor U56, or the according empty vector controls in LB with the appropriate antibiotics and 1% glucose. We then induced 250mL of each strain in triplicates at OD_{600nm} 0.05 and grew them until OD_{600nm} 0.3. (ca 2 h) on 0.3% arabinose and 10uM $MgSO_4$. At OD_{600nm} 0.3 we added 2mL of T5 phage to a final MOI of 5 to each of the cultures and sampled 50mL of the cultures after 5min, 15min, 30min, and 45 min respectively. To sample the lysates, we spun 50mL of culture at each timepoint at 4°C, transferred from falcon to Eppendorf, spun down again, and froze the pellet on Ethanol over dry ice. Samples were kept at -80°C until further analysis. Cell pellets were extracted in a mixture of MeOH, MQW and chloroform. The samples were vortexed and then flash-frozen in liquid nitrogen for 1 minute. Thawing and vortexing were repeated for four cycles to ensure proper suspension and breakage of the cell pellet. After vortex mixing and centrifugation (5 min at 15000g/ 4°C), the whole supernatant was evaporated under a gentle flow of N2. Finally, the aliquot was resuspended in a small volume of 50%B (HILIC) and filtered for polar analysis. The samples were then filtered (0.22 μm) and stable isotope-labeled standards were added before injection.

LC-MS

Sample analysis was carried out by MS-Omics as follows. The analysis was carried out using a Thermo Scientific Vanquish LC coupled to a Thermo Q Exactive HF MS. An electrospray ionization interface was used as an ionization source. Analysis was performed in negative and positive ionization mode. The UPLC was performed using a slightly modified version of the protocol described.[89] Peak areas were extracted using Compound Discoverer 3.3 (Thermo Scientific). Identification of NAD^+, ADPr and cADPr were performed at four levels; Level 1: identification by retention times (compared against in-house authentic standards), accurate mass (with an accepted deviation of 3ppm), and MS/MS spectra, Level 2a: identification by retention times (compared against in-house authentic standards), accurate mass (with an accepted deviation of 3ppm). Level 2b: identification by accurate mass (with an accepted deviation of 3ppm), and MS/MS spectra, Level 3: identification by accurate mass alone (with an accepted deviation of 3ppm). Manual extraction of the targeted compound signals was performed using Skyline 22.2 (MacCross Software) and FreeStyle 1.8 SP2 (Thermo Fisher Scientific). Data was corrected to calculate the original concentrations in the bacterial cytoplasm as previously described.[35] In brief, $OD_{600\ nm}$ was measured for the different strains' cultures (48 mL) at different times during infection, and the volume of the bacterial cytoplasm was calculated assuming an average cell volume of 10^{-15} L and a cell concentration of 10^9 cells/ml for an $OD_{600\ nm}$ of 1.0.

Structural biology

Negative staining sample preparation

Retron-Eco1 complexes were incubated with 1 mM of NAD^+ for 1 hour at 20° C in the ''cleavage'' buffer supplemented with $MgCl_2$. Samples were clarified by centrifugation at 13,000 × g for 10 minutes and injected in a Superose 6 Increase 3.2/300 column (Cytiva) equilibrated in the ''cleavage'' buffer supplemented with 5 mM $MgCl_2$.

Negative staining TEM

The oligomeric state of the complexes was assessed by negative staining transmission electron microscopy (TEM). C300Cu100 (quantifoil) grids were glow discharged for 30 sec at 15mA (10^{-3} mbar). Retron-Eco1 samples (3 μL) corresponding to the center of the SEC peaks (Figure S2A) were applied to the grids, and incubated for 1 min. The samples were fixed by incubation with 2% uranyl acetate. Images were collected on a CM100(b) TEM microscope (Philips), equipped with a LaB_6 emitter filament, and an Olympus Veleta camera (2048 x 2048 pixels), operated at 80keV and a nominal magnification of x 66000–98000. The average length of the particles was measured manually for ~200 particles or filaments using Fiji (ImageJ).

CryoEM sample preparation

The sample of Retron-Eco1-WT in complex with ADPr, was prepared by incubation with NAD^+ and subsequent purification as described above (see ''Negative staining sample preparation''). For the Retron-Eco1-WT sample, filamentous structures were enriched by collecting fractions from the 1.1 to 1.3 mL of the SEC chromatogram (Figure S2A). For the Retron-Eco1-WT+NAD^+, Retron-Eco1-E106A and Retron-Eco1 -1 turn mutant, we collected the fractions from the center of the peaks (Figure S2A). Freshly purified Retron-Eco1-WT, -E106A, and ADPr bound Retron-Eco1-WT and -1 turn mutant complexes (3μL at an absorbance at 260 nm of ∼9-12) were applied to R1.2/1.3 Cu300 grids (Quantifoil), glow-discharged for 60 s at 10 mA (Leica EM ACE200), and plunge-frozen in liquid ethane (pre-cooled with liquid nitrogen) using a Vitrobot Mark IV (FEI, Thermo Fisher Scientific) using the following conditions: blotting time 3 s, 100% humidity and 4 °C.

CryoEM data collection

A full description of the data collection parameters and processing workflow is available in Figures S2–S4 and Table S2. In brief, Retron-Eco1-WT, -WT+NAD^+, and -E106A mutant movies were collected with a Titan Krios G2 at 300keV equipped with a TFS Falcon III camera operated at 300 keV in counting mode at a magnification of x 96000 (0.832 Å/px) using a total dose of ∼40 e/Å2 (Figures S2–S4; Table S2). In the case of the Retron-Eco1 -1 turn mutant + NAD^+, movies were collected with a Titan Krios G2 at 300keV equipped with a TFS Selectris X energy filter, using a filter slit width of 5 eV, and a TFS Falcon 4i camera operated at 300 keV in counting mode at a magnification of x 165000 (0.725 Å/px) using a total dose of ∼50 e/Å2. (Figure S4; Table S2).

CryoEM data processing

All the data processing steps were performed in cryoSPARC (v4.2.1).[80] Movies were motion corrected (Patch motion correction, cryoSPARC) and the CTF was estimated (patch CTF estimation, cryoSPARC) with default parameters. Corrected exposures with a CTF fit < 4Å were selected for further processing. Particles were ''picked'' using a Topaz pre-trained model with ResNet8 (64 units).[90] Particles were extracted using a box size of 600x600 pixels for Retron-Eco1-WT and -E106A datasets. Retron-Eco1 -1 turn mutant particles were extracted using a box size of 686x686 pixels, to account for the difference in magnification. Extracted particles we 2D classified into ∼100 classes. Most of the classes converged into images showing 2D projections of the filament (Figures S2C, S3B, S4B, and S4F). Initial maps were obtained by Ab initio reconstruction using two classes for the Retron-Eco1-WT and Retron-Eco1-WT + NAD^+ complexes, or three for the Retron-Eco1-E106A and -1 turn mutant complexes. Maps containing density for what we attributed to Retron-Eco1 filaments were further refined to high resolution by applying a homogeneous refinement method, and further classified by using one or several rounds of heterogeneous refinement.

For Retron-Eco1-WT without ligand, we obtained one map at 4.41 Å resolution (Figure S2E, EMDB-18317), and a low-resolution map (3.8 Å) of the RT-dimer was also obtained (Figure S2F). For Retron-Eco1-WT+NAD^+, we obtained three maps: (1) A consensus refinement map at 3.13 Å resolution (EMDB-19793, Figure S3D), (2) a full map corresponding to two segments of the assembly at 3.09 Å resolution (EMDB-18315, Figure S3E) and (3) a local map cantered in one of the segments at 2.99Å resolution (EMDB-18313, Figures S3F and S3G). The last map was obtained by applying 3D classification without alignment (6 classes, cryoSPARC) using a mask centered in one of the segments (Figure S3F). These maps correspond to the different conformations displayed in Figures S3F and S9C and Video S1. For Retron-Eco1-E106A mutant, we obtained one full map corresponding to two segments of the assembly at 2.66 Å overall resolution (EMDB-18314, Figure S4D). For Retron-Eco1 -1 turn + NAD^+ mutant, we obtained one consensus refinement map at 2.43 Å resolution (EMDB-19792, Figure S4H). This map was used for comparison with the WT + NAD^+ consensus refinement (EMDB-19793, Figure S3D) in Figures 5B, S9A, and S9B. The conformational heterogeneity of this map was further analyzed by 3D classification without alignment (6 classes, cryoSPARC) using a mask centered in one of the segments (Figure S4I). These maps correspond to the different conformations displayed in Figures S4I and S9D and were used for comparison with the 6 classes obtained for WT+NAD^+ (Figure S3F). The additional map resembling the previously reported Retron-Eco1 dimeric structure (EMDB-22336) was also obtained from the -1 turn mutant processing (Figure S4J).

Possible duplicated particles were removed by applying a threshold of 160 Å before the last refinement step for the maps EMDB-18315 and EMDB-18313. CTF estimated per-particle was used for an accurate estimation of the defocus in the last refinement steps. Local resolution was calculated using cryoSPARC[80] and plotted into the final maps in Chimera X.[81] Sharpened maps were calculated using ''auto-sharpen map'' job in Phenix (v1.19-4092).[82]

Model building and refinement

The Retron-Eco1 RT (AF-P23070-F1) and a custom-made AF2 model for the Retron-Eco1-Effector were fitted into the cryoEM density in Chimera X v1.6.1.[81] Models for the ncRNAs and msDNA were generated with Ideal B-form in Coot v0.9.6[83] (''Ideal DNA/RNA''). The initial models for the RT, Effector, ncRNAs and msDNA were manually adjusted and refined in Phenix[82] against the map for Retron-Eco1-E106A. The resulting models were rigid body-fitted into the density of the extra copies in the filamentous assembly using ChimeraX,[81] and manually refined in Coot[83] applying self-molecule restraints generated at 5Å. The geometry was minimized by adding hydrogens and refinement in Phenix.[82] The refined model was used as input for building the Retron-Eco1-WT complexes. In brief, the initial model was rigid-body fitted into the Retron-Eco1-WT maps, manually adjusted in coot, and further refined in Phenix.[82] Restraints dictionaries were generated for NAD^+ and ADP-ribosylated-E106 (E99) molecules using GRADE2 server[84] and used for refinement (https://grade.globalphasing.org/). Hydrogens were removed and the final models were corrected in coot. Molecular figures were prepared in ChimeraX v1.6.1.[81] The surface conservation of molecular surfaces and the primary sequence was calculated with the Consurf server,[85] using multiple sequence alignements of the RT and effector proteins of 186 type II-A3 retrons previously described.[23] Primary sequence alignments displayed in this paper were performed with Consurf[85] or ESPript3[86] servers.

Map analysis with OccuPy

The local quality of the consensus refinement maps for Retron-Eco1-WT+NAD$^+$ and -1 turn mutant +NAD$^+$ was calculated by using OccuPy[54] with default kernel settings (kernel size: 9 pixels, kernel radius: 5.52 pixels) (Figure 5B). The apparent occupancy was calculated by low-pass filtration of the map at 15Å (Figure S9B). For the previously reported Retron-Eco1 dimeric structure[31] (EMDB-22336, Half map 1) and the related map obtained during the -1 turn mutant processing (Figure S4J), the local quality of the map was calculated using OccuPy[54] with default kernel settings (kernel size: 9 pixels, kernel radius: 4.71/5.52 pixels) (Figures S9F and S9G).

Detection of ADP-ribosylated proteins

Western blot

For the detection of ADP-ribosylated Retron-Eco1-effector, 0.5 μg of the recombinant complexes, or 5 μL of the bacterial culture at OD_{600nm} of 0.6 were denatured by addition of LDS reducing loading Buffer (Pierce). Samples were loaded in NuPage 4 to 12% gels (Invitrogen) and proteins were blotted onto a nitrocellulose membrane (iBlot™ Transfer Stack, Invitrogen). ADP-ribosylated targets were stained by incubation with an anti-Poly/Mono-ADPr antibody (E6F6A, Cell Signaling Technology, 1:1000, 1 h at 25 °CRT) in PBS supplemented with 0.1% tween (PBST) and 2% BSA, followed by incubation of a secondary peroxidase-conjugated antibody (1h, RT in PBST). Chemiluminescence was detected by SuperSignal™ West Pico PLUS Chemiluminescent Substrate (Thermo). The total protein content was detected by ponceau staining for the recombinant complexes, or by Coomassie staining for the bacterial cell samples. For hydroxylamine treatment, 2μM of Retron Eco1-WT was incubated with 1 mM NAD$^+$ for 90 min at 20 °C in cleavage buffer. Subsequently, 100 mM of HEPES (pH 9.0) was added and incubated ON at 20°C. The sample was further incubated with 1M NH_2OH ON at 20°C, and ADPr was detected by western blot using ADPr specific antibodies.[41]

Sample preparation for mass spectrometry

For analysis by MS, samples were incubated with 1 mM of NAD$^+$ for 90 min as described before (see "In vitro NAD$^+$ cleavage assays"). The sample was frozen at -20°C until the day of the MS experiment. Two sets of MS experiments were performed: an initial qualitative ("QL") experiment and a quantitative ("QN") experiment. All samples contained 2 μM of Retron-Eco1 complexes containing two proteins; Retron-Eco1reverse transcriptase (UniProt: P23070) and Retron-Eco1 putative ribosyltransferase/DNA-binding protein (UniProt: P0DV f88), buffered in 20 mM HEPES (pH 7.5), 200 mM KCl, and 1 mM TCEP. QL experiments included WT and E106A mutant retron-Eco1 ribosyltransferase. All experiments were performed with and without the addition of 1 mM NAD$^+$ for 90 min.

For QL samples, 10 μg of protein was digested using 1:100 (w/w) trypsin for 3 h at 25 °C. For QN samples, urea was added to a final concentration of 4 M (from 10 M stock) to 25 μg protein, buffered with 50 mM TRIS pH 7.0, digested with 1:100 (w/w) Asp-N protease for 5 hours at 25 °C, and further digested with 1:100 (w/w) Lys-C protease overnight at 25 °C. Following digestion, all samples were reduced and alkylated for 1 hour at 25 °C by concomitant addition of chloroacetamide and tris(2-carboxyethyl)phosphine (TCEP) to a final concentration of 5 mM, and filtered through 0.45 μm spin filters to clear any debris prior to StageTip purification of peptides. C18 StageTips were prepared in-house, by layering four plugs of C18 material (Sigma-Aldrich, Empore SPE Disks, C18, 47 mm) per StageTip. Activation of StageTips was performed with 100 μL 100% methanol, followed by equilibration using 100 μL 80% acetonitrile (ACN) in 0.1% formic, and two washes with 100 μL 0.1% formic acid. Samples were acidified to pH <3 by addition of trifluoroacetic acid to 1% (v/v), after which they were loaded on StageTips. Subsequently, StageTips were washed twice using 100 μL 0.1% formic acid, after which peptides were eluted using 80 μL 25% ACN in 0.1% formic acid. All fractions were dried to completion using a SpeedVac at 60 °C. Dried peptides were dissolved in 20 μL 0.1% formic acid (FA) and stored at −20 °C until analysis using mass spectrometry (MS).

Mass spectrometry data acquisition

All samples were analyzed on an EASY-nLC 1200 system (Thermo) coupled to an Orbitrap Fusion™ Lumos™ Tribrid™ mass spectrometer (Thermo). Samples were analyzed on 20 cm long analytical columns, with an internal diameter of 75 μm, and packed in-house using ReproSil-Pur 120 C18-AQ 1.9 μm beads (Dr. Maisch). The analytical column was heated to 40 °C, and elution of peptides from the column was achieved by application of gradients with stationary phase Buffer A (0.1% FA) and increasing amounts of mobile phase Buffer B (80% ACN in 0.1% FA). The primary analytical gradients ranged from 5 %B to 50 %B over 30 min for QL samples, and 5 %B to 42 %B over 65 min for QN samples. Electrospray ionization (ESI) was achieved using a Nanospray Flex Ion Source (Thermo). Spray voltage was set to 2 kV, capillary temperature to 275 °C, and RF level to 30%. Full scans were performed at a resolution of 120,000, with a scan range of 350 to 1,350 m/z (QL) or 400 to 1,400 m/z (QN), a maximum injection time of 50 ms, and an automatic gain control (AGC) target of 600,000 charges ("150" normalized AGC target). Precursor isolation was performed at a width of 1.3 m/z, an AGC target of 200,000 charges ("400" normalized AGC target), and precursor fragmentation was accomplished using electron transfer disassociation with supplemental higher-collisional disassociation (EThcD) at 20 NCE, using calibrated charge-dependent ETD parameters. Charge-dependent ETD calibration resulted in ETD activation times of 99.56 or 100.28 ms for z=2 precursors, 44.25 or 44.57 ms for z=3 precursors, 24.89 or 25.07 ms for z=4 precursors, 15.93 or 16.05 ms for z=5 precursors, and 11.06 or 11.14 ms for z=6 precursors, for QL and QN runs, respectively. This equates to an ETD Time Constant (τ) of 2.21 or 2.23, respectively. Precursors with charge state 2-6 were isolated for MS/MS analysis, with priority given to any z=3-6 precursors, prior to considering z=2 precursors. Selected precursors were excluded from repeated sequencing by setting a dynamic exclusion of 30 seconds (QL) or

60 seconds (QN). MS/MS spectra were recorded in the Orbitrap, with a loop count (TopN) setting of 3, a maximum precursor injection time of 250 ms, a minimum intensity threshold of 80,000 charges/second, and a scan resolution of 60,000.

Mass spectrometry data analysis

All RAW files were analyzed using MaxQuant software (version 1.5.3.30),[91] in a single computational run. Default MaxQuant settings were used, with exceptions outlined below. For generation of the theoretical spectral library, all expected full-length protein sequences (UniProt: P23070 and P0DV88, as well as P0DV88 with E106A mutation) were entered into a FASTA database. QL samples were assigned to Parameter Group 0, and QN samples to Parameter Group 1. For QL data, in silico digestion was performed using "Trypsin/P" in semi-specific mode (which allows non-specific cleavage on either end of the peptide). For QN data, in silico digestion was performed using "LysC/P", "AspN", and "GluN" (to accommodate off-target activity of Asp-N), in a semi-specific mode. Minimum and maximum peptide length were set to 6 and 60, respectively. For all data, protein N-terminal acetylation (default), oxidation of methionine (default), deamidation of asparagine and glutamine, peptide N-terminal glutamine to pyroglutamate, carbamidomethylation of cysteine, and ADP-ribosylation of C/D/E/H/K/R/S/T/Y, were included as potential variable modifications, with a maximum allowance of 3 variable modifications per peptide. Precursors above z=6 were not considered. Modified peptides were stringently filtered by setting a minimum score of 80, a minimum delta score of 40, and a site decoy fraction of 0.02. Second peptide search was enabled (default). Matching between runs was enabled with a match time window of 2 min and an alignment time window of 20 min, matching of unidentified features, and with matching disallowed between QL and QN runs. Data was filtered by posterior error probability to achieve a false discovery rate of <1% (default). The mass spectrometry proteomics data for the ADPr have been deposited to the ProteomeXchange Consortium via the PRIDE partner repository with the dataset identifier PXD044835.

Growth curves with msDNA mutants

E. coli MG1655 (DE3) carrying the pET21a-RT-ncRNA and pACYC-Duet-Effector for the WT and mutants were grown ON in LB media supplemented with 5 mM $MgCl_2$. The next morning, the culture was diluted 1:100 in LB supplemented with 5mM $MgCl_2$ and grew until a OD_{600nm} of 0.2. at 37°C. Then, cells were transferred to the wells of a 96-well plate (Thermo), and the mutant's expression was induced by addition of 0.1 mM IPTG. The growth was monitored over time by measuring OD_{600nm} in a Tecan flash plate reader with the following parameters: 37°C, 200 rpm, 300 min.

Phage escaper analysis

Phage escaper sequencing

We extracted the total DNA from the escaper phages lysate after enrichment for high phage titer (> 10^7 pfu/ mL) DNA with the DNeasy blood and tissue kit (QIAGEN), starting from the Proteinase-K treatment step to lyse the phages.[92] We used next generation sequencing to next-generation analyze the genome of sequenced the escaper phages (Illumina Novaseq 6000, Novogene Co LTD) and analyzed their genomes in comparison to the ancestor phage with breseq 0.37.0[87] to identify mutations in the genomes. As the duplicated region could not be sufficiently mapped to the ancestor phages, we PCR amplified that region and long-read sequenced it (Oxford Nanopore; PlasmidSaurus LLC).

U69 toxicity assay

We co-transformed plasmids carrying U69 and Eco1 respectively, alongside the according empty vector controls, into *E. coli* NEB5a and recovered and plated the cells with the appropriate selective antibiotics. We then picked 12 colonies of each transformation and grew them in 150ul of LB media each supplemented with the appropriate antibiotics in a 96-well plate. We monitored the OD_{600nm} over 5.5h in 2-minute intervals and visualized the end-point data in Figure 5B. Note, as we could observe a toxic effect of U69 alone when induced during cloning, we supplemented the media in all steps with 1% glucose.

Structure comparison of U55 and Tad1

Genes present in the duplicated region of Ukendt phage were used as queries for homology searches against known anti-defense proteins. Sequence-based searches did not render any significant results. However, structure-based searches using predicted structures with AlphaFold2[63] and TM-align[93] revealed strong similarities between the gene ukendt_55 and the N-terminal region of Tad1 (PDB: 7AUW), with RMSD values below 2.7 and TM-scores above 0.5. To rule out the confounding factor of the structural prediction itself, we decided to compare both with a close homolog of ukendt_55 present in the phage anhysbys, obtaining similar values.

Isothermal titration calorimetry

Adenosine 5′-diphosphoribose sodium salt (ADPr) was purchased from Merck (A0752). Prior to ITC experiments U56 was extensively dialyzed against ITC buffer, 20 mM potassium phosphate pH 7.5, 300 mM KCl, 1 mM TCEP and the ADPr diluted to the working concentration in the ITC buffer. All ITC experiments were performed on an Auto-iTC200 instrument (Microcal, Malvern Instruments Ltd.) at 25 °C. U56 concentration was determined using a spectrophotometer by measuring the absorbance at 280 nm and the extinction coefficient computed from the corresponding sequence by the ProtParam program (http://web.expasy.org/protparam/). The ADPR concentration was determined as well by measuring the absorbance at 260 nm and using an extinction coefficient of 15640 M^{-1} cm^{-1}. ADPR at approximately 450 μM concentration was loaded into the syringe and titrated into the calorimetric cell containing U56 ~ 30 μM. The reference cell was filled with distilled water. In all assays, the titration sequence consisted of a single 0.4 μl injection followed by 19 injections, 2 μl each, with 150 s spacing between injections to ensure that the thermal power returns to the baseline

before the next injection. The stirring speed was 750 rpm. Control experiments with ADPR injected in the sample cell filled with buffer were carried out under the same experimental conditions. These control experiments showed negligible heats of dilution. A single-site model was fitted to the heats per injection normalized per mole of injectant versus the molar ratio [ADPR]/[U56]. Data were analyzed with MicroCal PEAQ-ITC (version 1.1.0.1262) analysis software (Malvern Instruments Ltd.). Initial fitting of the data yielded stoichiometry values of ~0.5, suggesting a 2:1 U56:ADPr stoichiometry. The final analysis was performed by fitting a single-site model to the data using the concentration of the U56 dimer and ADPr monomer.

DNA ADP-ribosylation

Immuno-detection of ADP-ribosylated DNA

25 mL of MG1655(DE3) transformed with pET21a -RT-ncRNA and pACYC-Duet-Effector (WT and mutant) plasmids were grown in LB media, supplemented with 0.5% (w/v) glucose, 5 mM $MgCl_2$, 34 μg/mL of chloramphenicol and 100 μg/mL of ampicillin to a OD_{600nm} of 0.3. The expression of the Retron-Eco1 recombinant complexes was induced by incubation with 0.1 mM IPTG for 3h at 37°C. For expression experiments of Retron-Eco1 and U56 (Figure 7F), U56 was cloned in the second multicloning site of pACYC-Duet-Effector, and the expression was induced as described above. The bacterial DNA was extracted based on the protocol described in[17] with minimal modifications. In brief, bacteria were harvested by centrifugation (4000 x g, 3 min) and resuspended in 200 μL of phosphate-buffered saline (PBS) buffer supplemented with 100 μg/ml of RNAseA and incubated for 5 min at 20°C. Cells were lysed by addition of 200 μL of 2x boiling lysis buffer (2.0% SDS, 20 mM TRIS-Cl, 2 mM EDTA, pH 8.0) and heating to 95°C for 5 min. The lysate was incubated with 2.5 μL of proteinase K (100 μg/mL) for 1 h at 50°C. gDNA was purified by using phenol: chloroform protocol followed by precipitation with sodium acetate and ethanol. The DNA pellet was vacuum concentrated (SpeedVac) and resuspended in H_2O to a final concentration of 300 ng/μL. Additional RNA contamination was removed by incubation with 100 μg/mL of RNAseA for 5 min before the blotting. 300 ng of DNA was dotted onto a Nylon membrane (0.45 micron, Roche) and crosslinked with 1800 J by using a Stratalinker UV crosslinker. Crosslinked DNA was stained with red safe (Sigma Aldrich) for total DNA. ADP-ribosylated targets were detected as described above ("Detection of ADP-ribosylated proteins – WB") by using an anti-Poly/Mono-ADPr antibody (E6F6A, Cell Signaling Technology). The quantification of DNA-ADPr labelling ratio was determined by densitometric analysis ADP-r labelled dots and normalized by the total concentration of DNA stained with red-safe staining. To verify the ADP-ribosylation of the bacterial DNA, 3.5 μg of the extracted bacterial DNA sample as used for the dot blots were run in a 1% agarose gel (E-Gel Agarose Gels with SYBR Safe DNA Gel Stain, Invitrogen) for 20 minutes. The gel was imaged upon illumination with UV light to account for the total amount of DNA. The contents of the gel were then transferred for 5 min to a Nylon membrane (iBlot-DNA Transfer Stack, Invitrogen) following the manufacturer's instructions. DNA was cross-linked to a nylon membrane, and ADP-ribosylated DNA was detected using the anti-ADPr antibody in the same manner as described for the dot-blot assays.

In vitro *ADP-ribosylation experiment*

Eight fluorescein-labelled (FAM) oligonucleotides of different sequences (2 μM) were incubated with the recombinant Retron-Eco1 -1 turn mutant (8 μM) in "cleavage" buffer supplemented with 5 mM $MgCl_2$ in the absence or presence of NAD^+ (1 mM) for 2 hours at 30°C. Then, Retron-Eco1 proteins were removed by incubation with proteinase K (0.5 μg/ml) for 30 min at 50°C. Subsequently, the DNAs were denatured by incubation at 95°C for 10 minutes, and the size of the nucleic acids was estimated by denaturing electrophoresis using TBE-Urea gels (10%, Novex) run according to the manufacturer's specification.

In vitro *U56 hydrolase experiment*

ADP-ribosylated DNA produced by expression of the -2 turn mutant (3μg), was incubated with U56 (10μM) for >16 hours at 25°C in "hydrolase" buffer (20 mM HEPES pH 7.5, 150 mM KCl, 1 mM EDTA). Then, U56 protein was removed by incubation with proteinase K (0.5 μg/ml) for 30 min at 50°C. Detection of ADP-ribosylated targets was performed as described above ("Immuno-detection of ADP-ribosylated DNA").

QUANTIFICATION AND STATISTICAL ANALYSIS

Quantification was performed a described in the methods section. Statistical analyses were performed in Prism 10 following the statistical approach suggested for each specific type of data. The specific statistical tests and the statistical parameters are reported in the figure legends.